Figures and figure supplements

The transpeptidase PBP2 governs initial localization and activity of the major cell-wall synthesis machinery in *E. coli*

Gizem Özbaykal *et al*

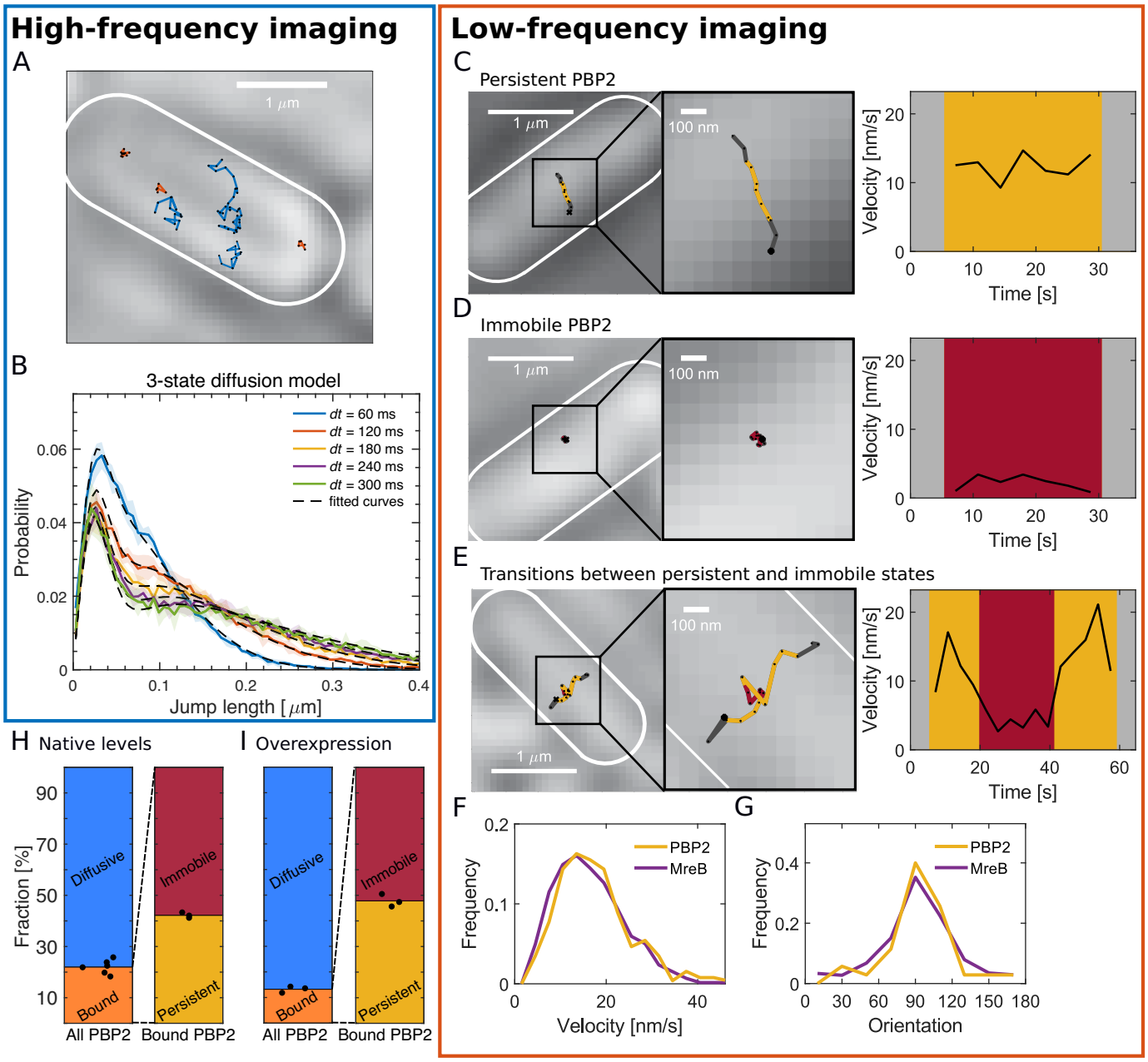

Figure 1. PBP2 molecules reside in diffusive, immobile, or persistently moving states. (**A**) Representative trajectories of PAmCherry-PBP2 molecules (TKL130) obtained by high-frequency imaging (time interval 60 ms) reveals diffusive (blue) and bound (orange) molecules. (**B**) Probability distribution of single-molecule jump lengths (solid lines, colored) and fit (dashed, black) using a three-state-diffusion model for different time intervals. 78% of PBP2 move diffusively with $<D> = 0.042\ \mu m^2/s$ while 22% are immobile. The shaded area indicates standard deviation between six biological replicates. (**C–E**) Low-frequency imaging (3.6 s with 1 s exposure time) reveals that bound PBP2 molecules are either persistently moving (**C**) or immobile (**D**), according to the instantaneous PBP2 velocity. PBP2 molecules show transitions between persistent and immobile states (**E**). (**F–G**) Persistently moving PBP2 and MreB filaments show similar speeds (**F**) and orientations of motion (orientation measured with respect to the cell centerline) (**G**). (**H–I**) Average fractions of bound, diffusive, persistently moving, and immobile PAmCherry-PBP2 at native levels (TKL130) (**H**) or if overexpressed (TKL130/pKC128) (**I**). Dots show biological replicates.

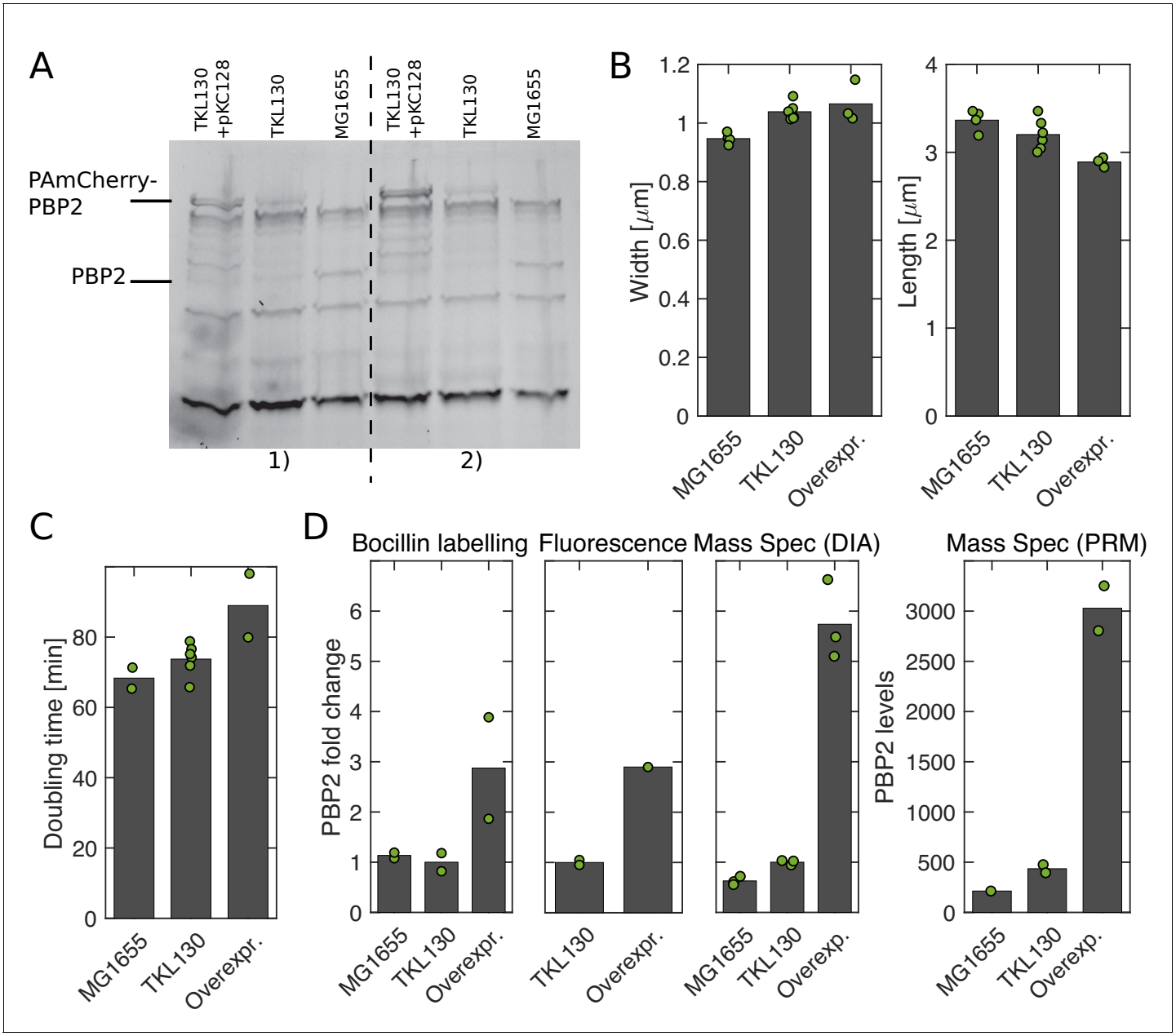

Figure 1—figure supplement 1. Comparison of PBP2-PAmCherry expressing cells and WT. (**A**) Bocillin-binding assay to compare expression levels of PBP2 in the wild-type strain (MG1655), the strain expressing PBP2-PAmCherry from the native locus (TKL130), and the strain overexpressing PBP2-PAmCherry (TKL130/pKC128). Quantification in (**D**). (**B**) Average cell dimensions obtained by phase-contrast microscopy and computational image segmentation. (**C**) Average doubling times during steady-state exponential growth in batch culture (from OD600). (**D**) Different methods to compare PBP2 expression levels in different strains (from left to right): Bocillin labeling (from A), single-cell fluorescence levels measured in epi-fluorescence mode, mass spectrometry [Data Independent Acquisitions (DIA) and Parallel Reaction Monitoring (PRM)]. For the first three methods, PBP2 levels are normalized by the corresponding value in TKL130. For PRM, we obtained absolute numbers of proteins per cell by comparing to reference peptides and colony counting. With both mass spectrometry methods, we observe a higher fold-change than through the other methods. Dots represent biological replicates.

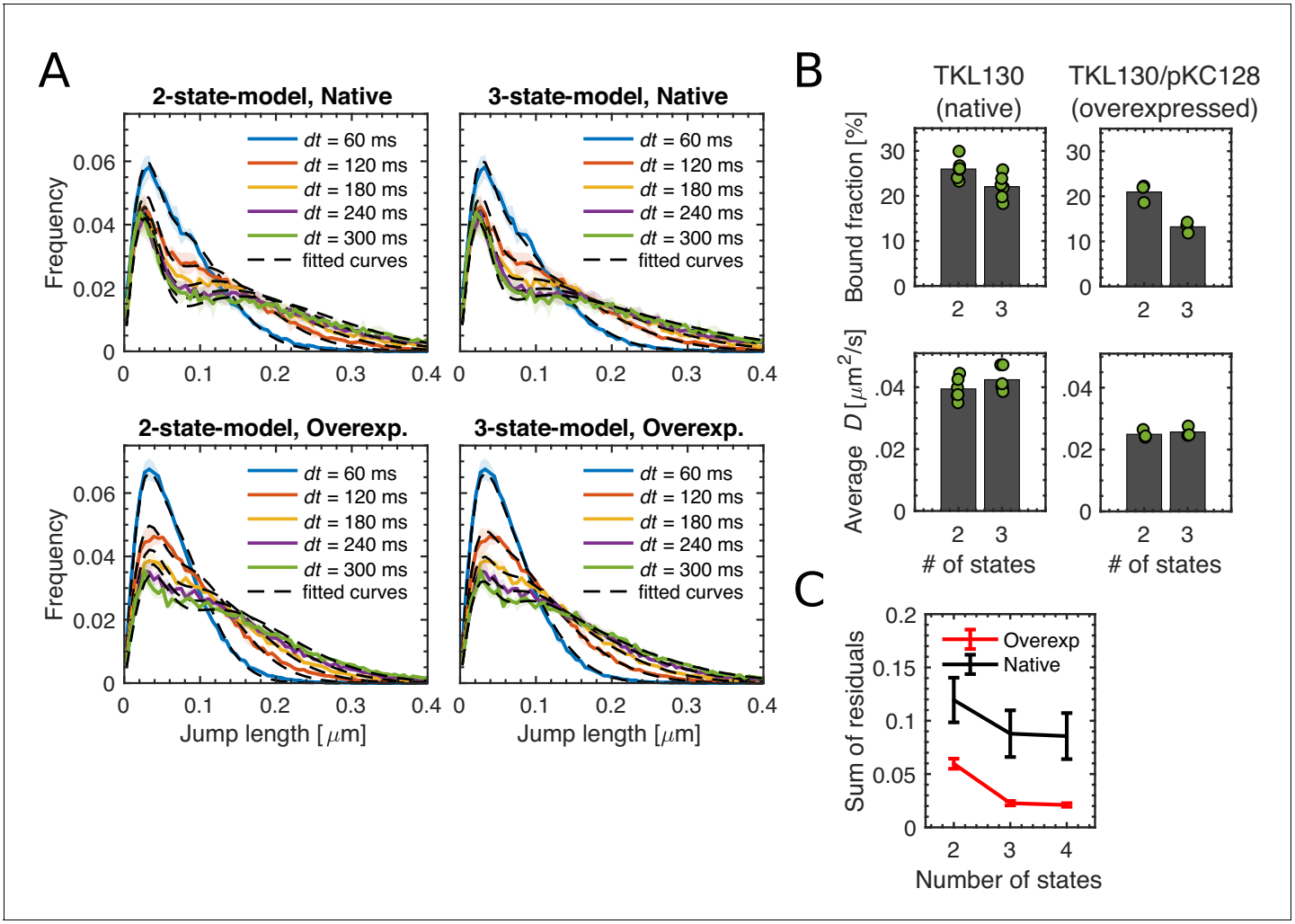

Figure 1—figure supplement 2. Comparing 2- and 3-state-diffusion models to fit experimental data through Spot-On. (**A**) Probability distributions of single-molecule jump lengths (solid lines, colored) and fit (dashed, black) using a two-state (left) or three-state (right) diffusion model for different time intervals for native levels (TKL130) and for over-expression (TKL130/pKC128) of PBP2-PAmCherry. Shaded regions show standard deviations between biological replicates. (**B**) Comparison of bound fractions and average diffusion constants acquired by fitting two-state and three-state diffusion models shown in (**A**). Dots represent biological replicates. (**C**) Normalized sum of residuals found by using multi-state models with Spot-On. Error bars show standard error between biological replicates.

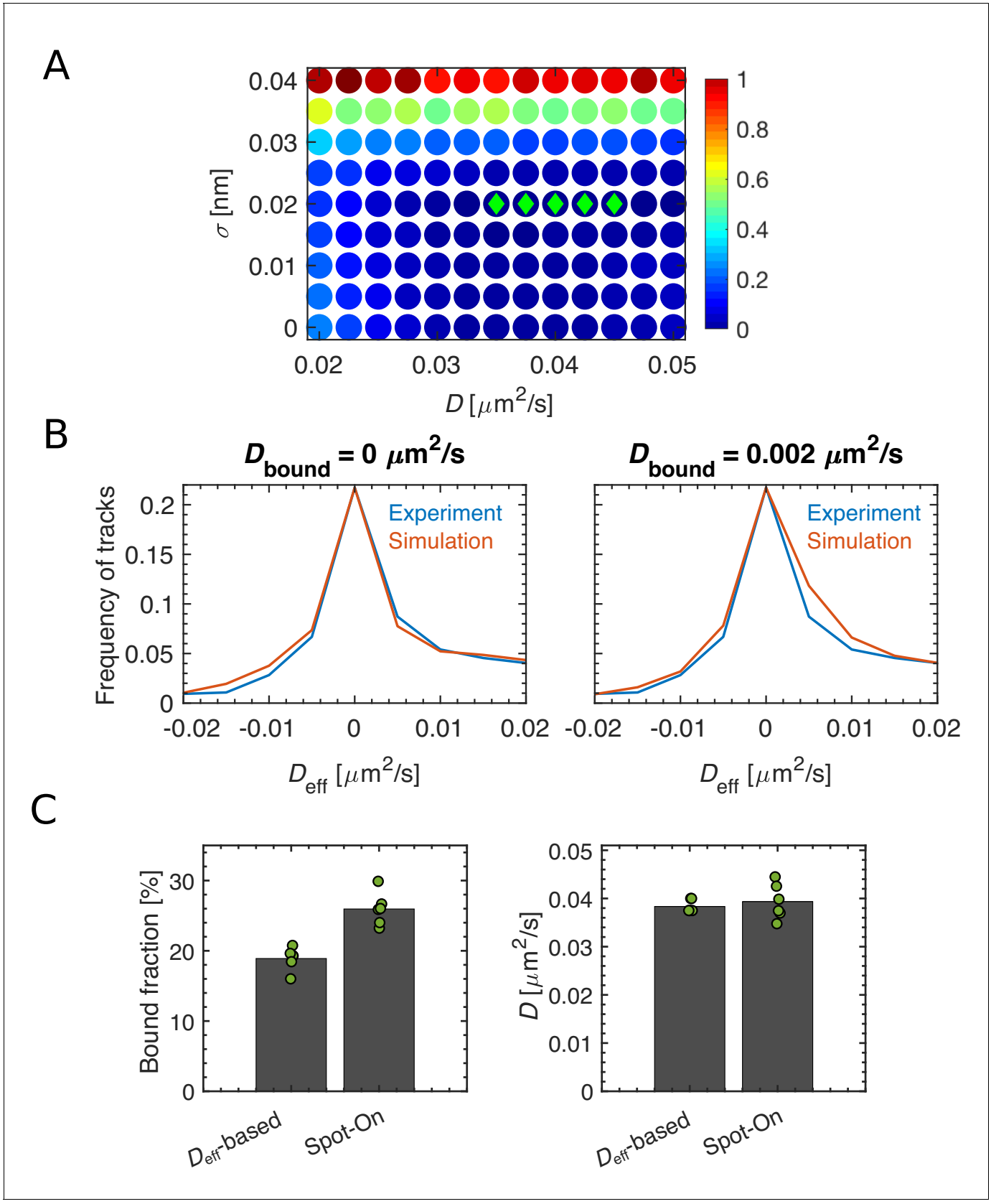

Figure 1—figure supplement 3. An alternative approach to fit a two-state diffusion model, based on the distribution of effective diffusion constants. (**A**) Heat map of sum of squared differences (RSS) between the D_{eff} distributions of single-track effective diffusion constants D_{eff} obtained from

Figure 1—figure supplement 3 continued on next page

Figure 1—figure supplement 3 continued

experimental data or computational simulations of a two-state model, using different model parameters D (diffusion constant of the diffusive fraction) and σ (localization precision). Parameter sets giving the lowest 5 RSS values are shown with green diamonds. Best fit is given by D = 0.04 $\mu m^2/s$ and σ = 20 nm. (**B**) We verified that the non-diffusive population was indeed not diffusing, with D_{bound} = 0 $\mu m^2/s$ (left), while a finite diffusion constant D_{bound} > 0.002 um^2/s gives poor agreement between simulation and experiment. Here, the experimental D_{eff} distribution is the mean of 6 biological replicates. (**C**) We compared the results of our method with the Spot-On code (2-state model) in TKL130 (native levels) and TKL130/pKC128 (overexpression), respectively.

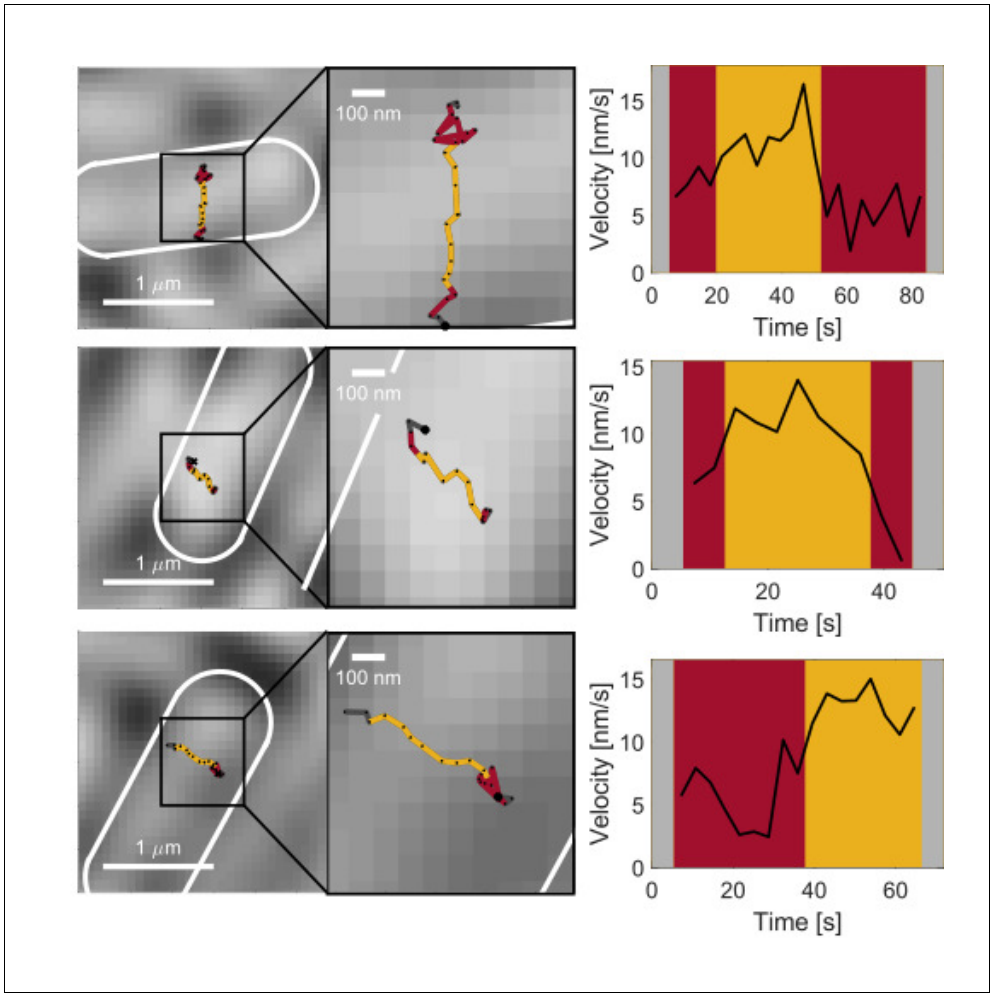

Figure 1—figure supplement 4. Transitions between immobile and persistent states. Example tracks and velocity as a function of time for example tracks that show transitions between persistent and immobile states.

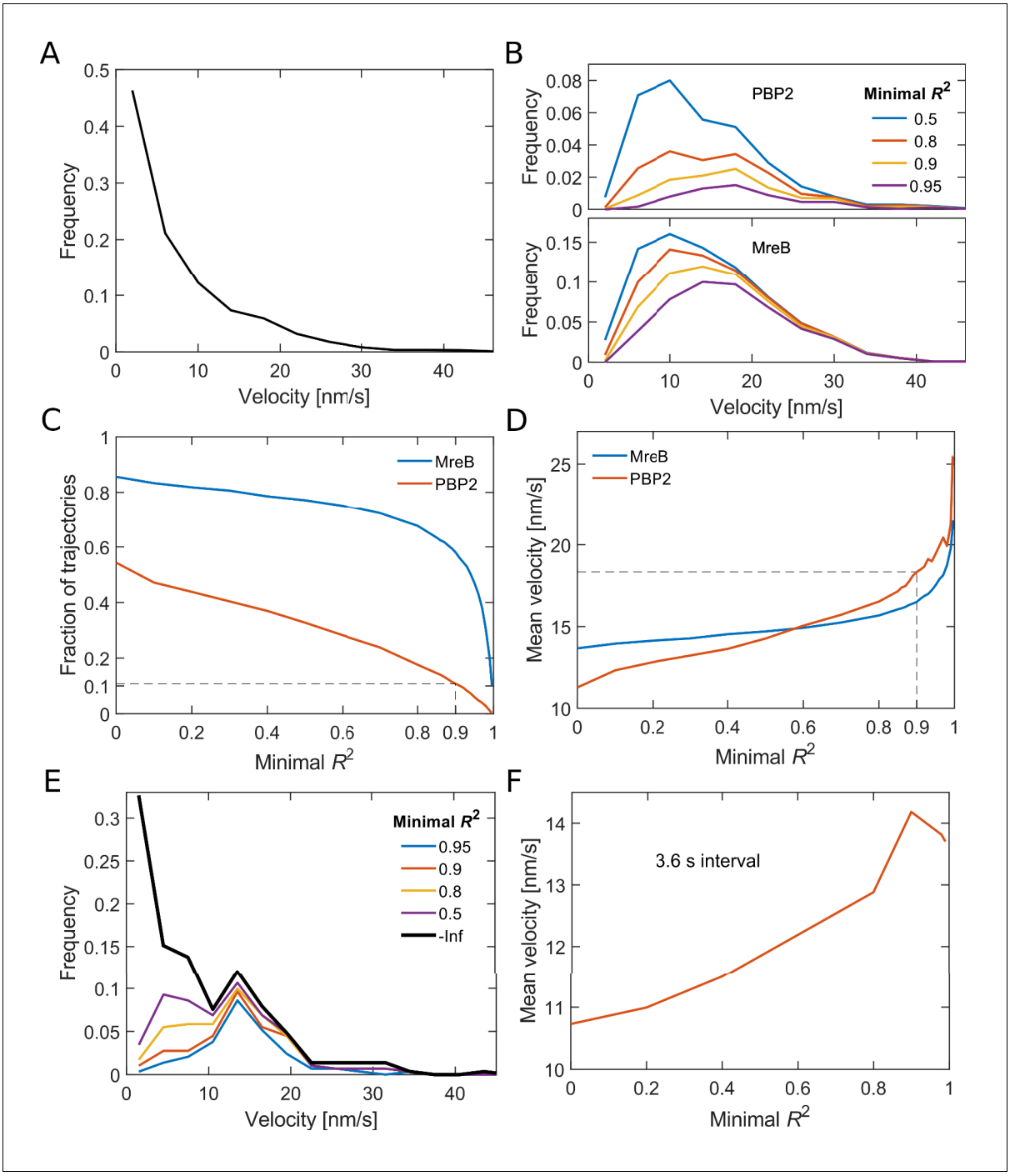

Figure 1—figure supplement 5. Analysis of bound PAmCherry-PBP2 molecules. (**A**) Velocity distribution of all PBP2 tracks measured with 1 s intervals. The velocity of individual tracks was determined by fitting a quadratic function to the MSD. (**B**) Velocity distributions for directed trajectories of PBP2 and MreB as found by selecting for an increased goodness of fit measured by R^2 of a quadratic function to the MSD. (**C**) The stricter the goodness of fit criterion (minimal R^2) the less trajectories contribute to the mean track velocity. (**D**) The mean velocity increases with increasing minimum R^2. The dashed line indicates the value chose for the distributions in ***Figure 1***. (**E–F**) The same analysis applied on 4-step segments of trajectories measured with 3.6 s intervals delivers smaller mean velocities, likely because fast trajectories reside for a shorter amount of time in the field of view.

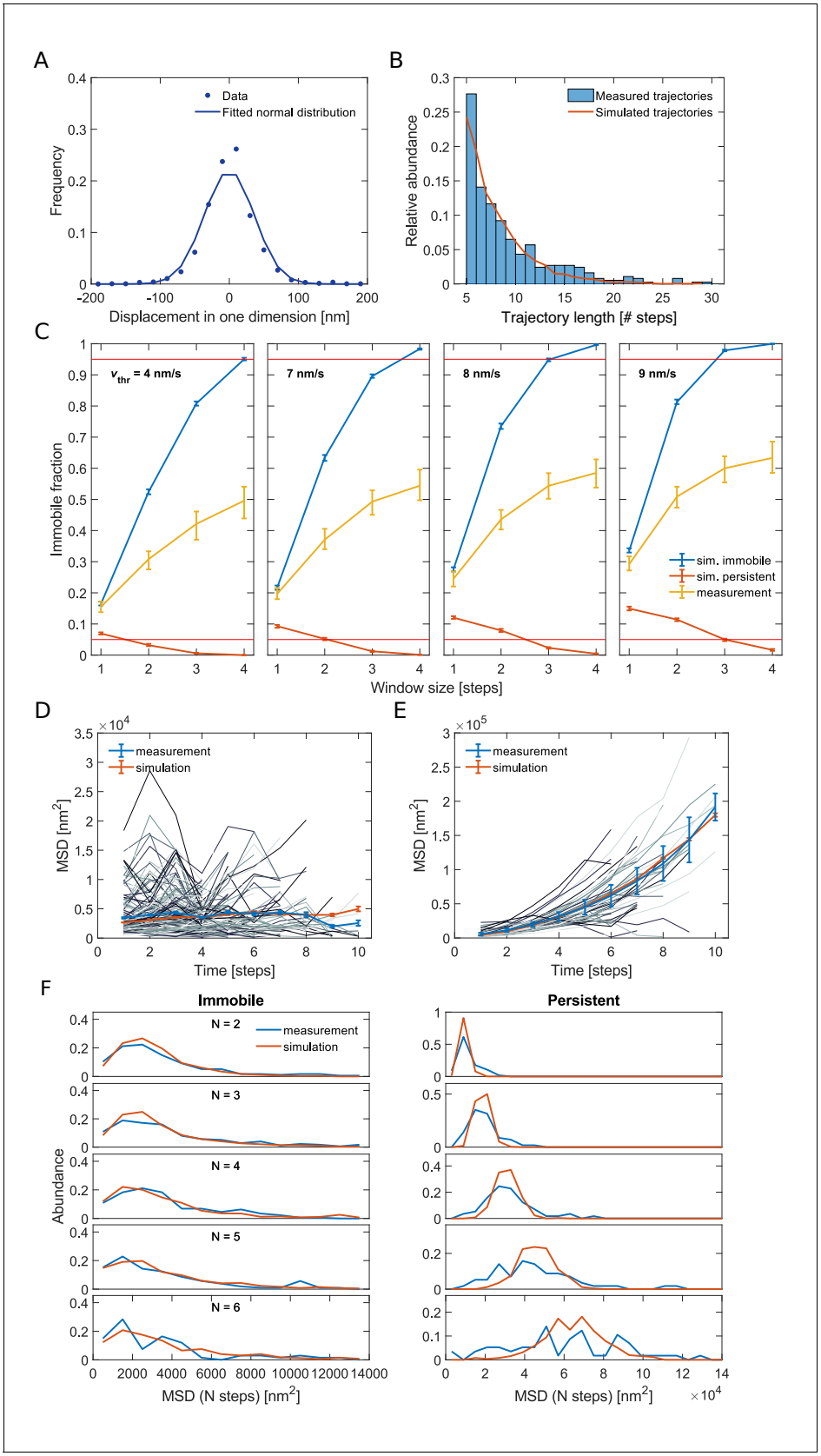

Figure 1—figure supplement 6. Quantitative analysis of persistent and immobile states based on computational simulations. (**A**) Distribution of measured single-step displacements in one dimension. A fit of a normal distribution to the data delivers a standard deviation of 36 nm, which

Figure 1—figure supplement 6 continued on next page

Figure 1—figure supplement 6 continued

corresponds to a localization error of single localization events of 25 nm. (**B**) We computationally simulated trajectories such that the length distribution of the simulated trajectories resembles the one from measured trajectories. (**C**) Fraction of immobile segments measured in simulations of immobile (blue) or persistent (red) molecules and in experimentally measured tracks (yellow) as a function of the moving-average window size and for different velocity thresholds. The red horizontal lines signify 5% and 95% probability thresholds, respectively. Error bars are from bootstrapping. For a window size of 4 steps and a velocity threshold of 8 nm/s the rate of wrong annotation is smaller than 1% both in simulations of purely persistent or immobile molecules. For pairs of w and v_{thr} that lead to high accuracy of the determination of immobile and persistent segments the immobile fraction of the experimental data shows similar results. (**D–E**) MSD's of single-track segments (gray lines) classified as (**D**) immobile or (**E**) persistent compared to the MSD of all respective segments (blue line). For simulated trajectories that can switch between the immobile and the persistent state (simulated with v = 12 nm/s, k_{ip} = 0.015 s^{-1}, k_{pi} = 0.021 s^{-1}) we find a similar behavior of the MSD curves (red line). (**F**) Distribution of MSD's of immobile and persistent segments for different numbers of steps N.

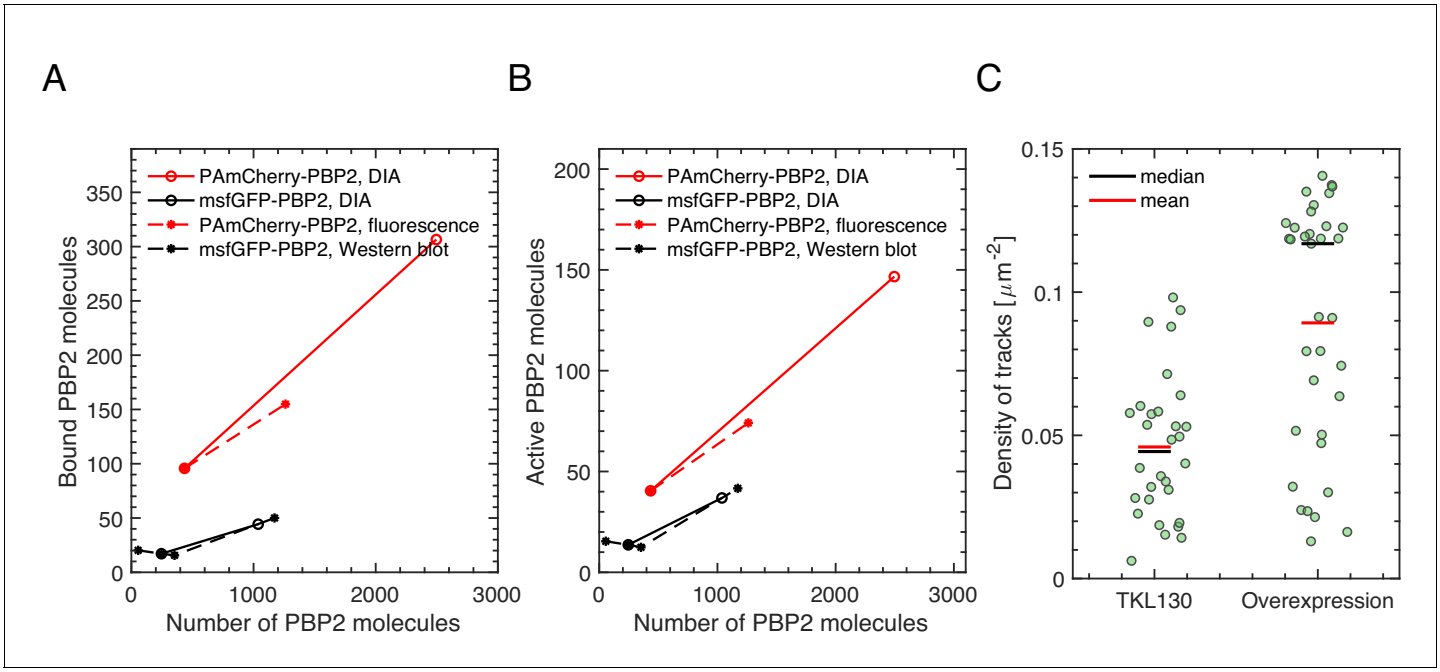

Figure 1—figure supplement 7. Number of bound PBP2 molecules increases with increasing PBP2 levels. (**A–B**) Number of bound PBP2 molecules ($N_{\mathrm{bound}} = N_{\mathrm{PBP2}}b$) (**A**) and active PBP2 molecules ($N_{\mathrm{active}} = N_{\mathrm{PBP2}}bp$) (**B**) as a function of the number of PBP2 molecules per cell (N_{PBP2}). *b* and *p* are the bound and persistent fractions of molecules, respectively. Since DIA, fluorescence, and Western Blot results only gave relative changes of PBP2 numbers, we used PRM values for TKL130 (for PAmCherry-PBP2) or for TU230(attLHC943) with 5 μM IPTG induction (for msfGFP-PBP2), respectively. (**C**) Density of tracks obtained by slow tracking for TKL130 and TKL130/pKC128, using same photo-activation and imaging conditions. Dots represent single fields of view (40 × 40 um). Despite variations between different fields of view, the fold-change of the median is of the same order as the relative change of bound molecules obtained in (**A**).

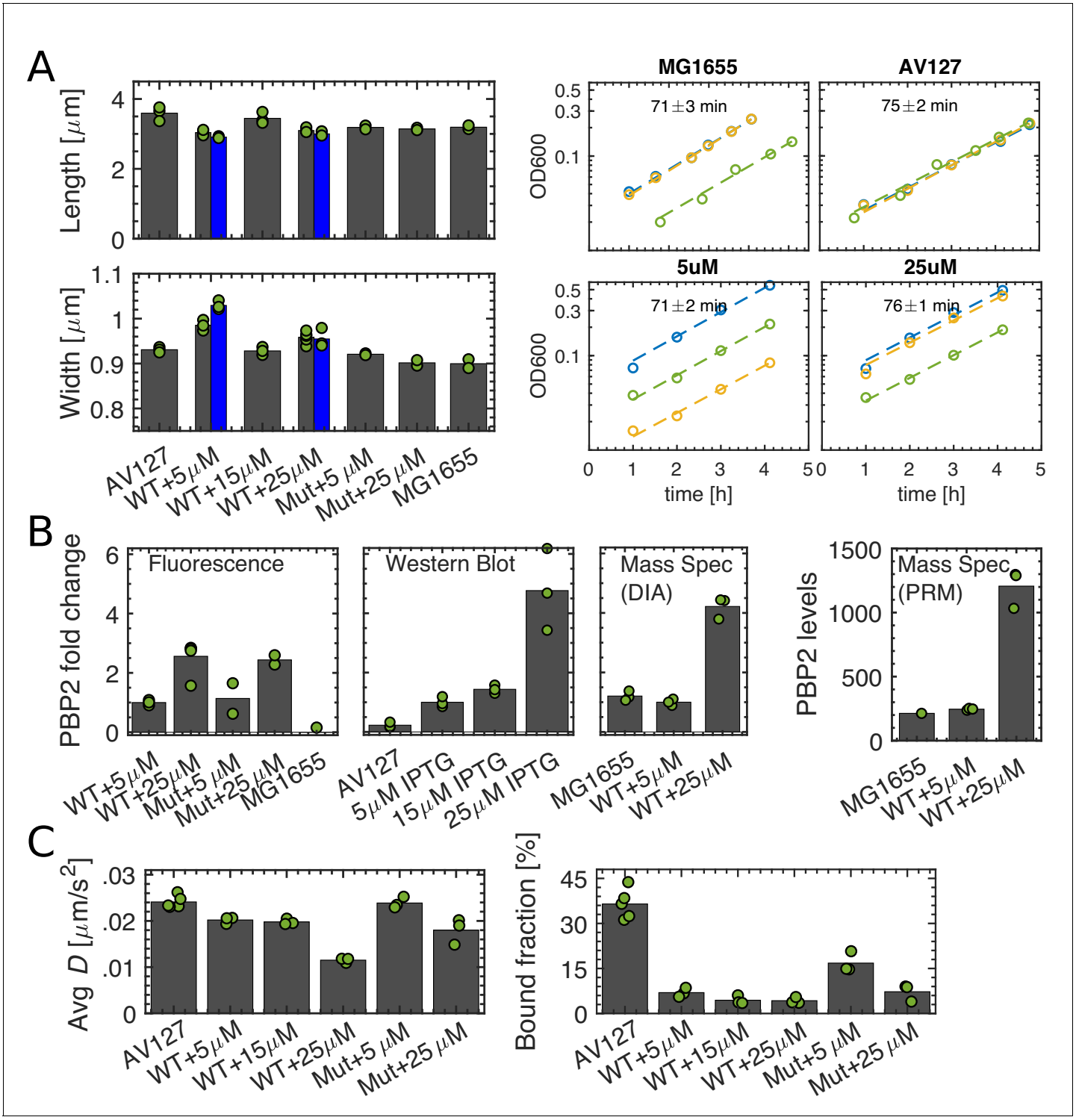

Figure 1—figure supplement 8. Comparison of AV127, msfGFP-PBP2 (TU230(attLHC943)), msfGFP-PBP2(L61R) (TU230(attLHC943)), and WT strains. (**A**) Length (top left), width (bottom left), and growth curves (right) of the strains carrying msfGFP-PBP2 (AV127 or IPTG-inducible) and msfGFP-PBP2(L61R) (labeled 'Mut') for different induction levels in comparison to MG1655. Gray and blue bars show cell dimensions after 6 and 10 hr of growth, respectively (see also ***Figure 1—figure supplement 9***). Doubling times are obtained from exponential fits (dashed lines) to three biological replicates (different colors). (**B**) PBP2 fold changes acquired from epi-fluorescence images, GFP-Western Blotting, and mass spectrometry measurements (DIA and PRM). The values are normalized by the value acquired from 5 μM IPTG induction except for PRM counts. PRM measurements combined with colony counting yield absolute numbers of proteins per cell. (**C**) Average diffusion constants and bound fractions. Gray bars show data after 6 hr of growth. Dots represent biological replicates.

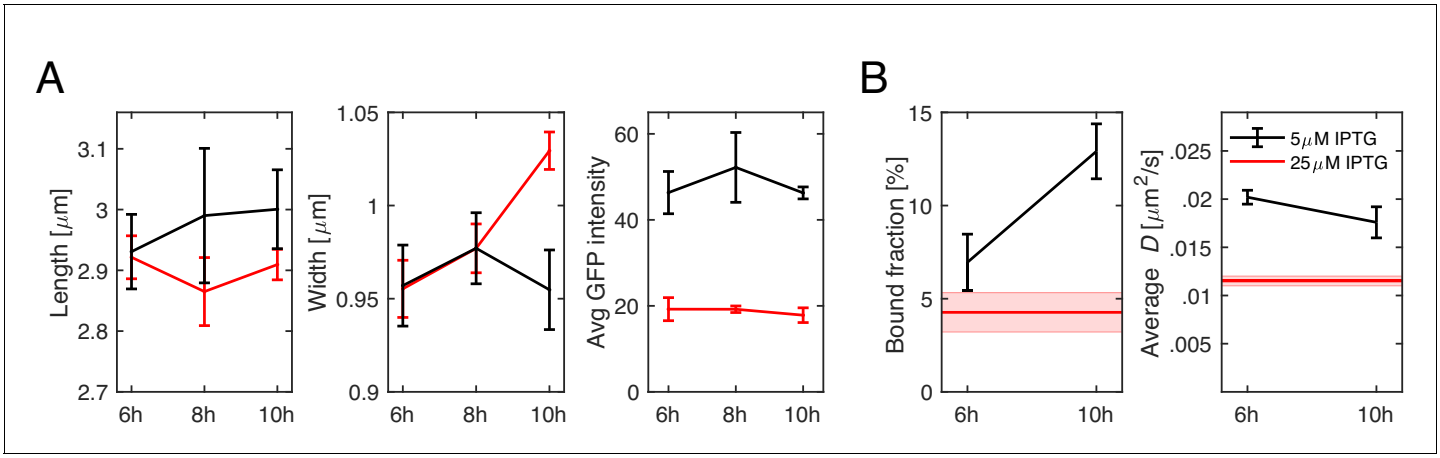

Figure 1—figure supplement 9. Time-dependent effect of low msfGFP-PBP2 expression. (**A**) Cell length, width, and GFP intensity as a function of time of TU230(attLHC943) cells for two different induction levels of 5 μM IPTG (black) and 25 μM IPTG (red). (**B**) Bound fractions and average diffusion constants. Red lines in (**B**) indicate the values measured for 25 μM induction during steady-state growth. Shaded areas and error bars show standard deviation between at least three technical replicates.

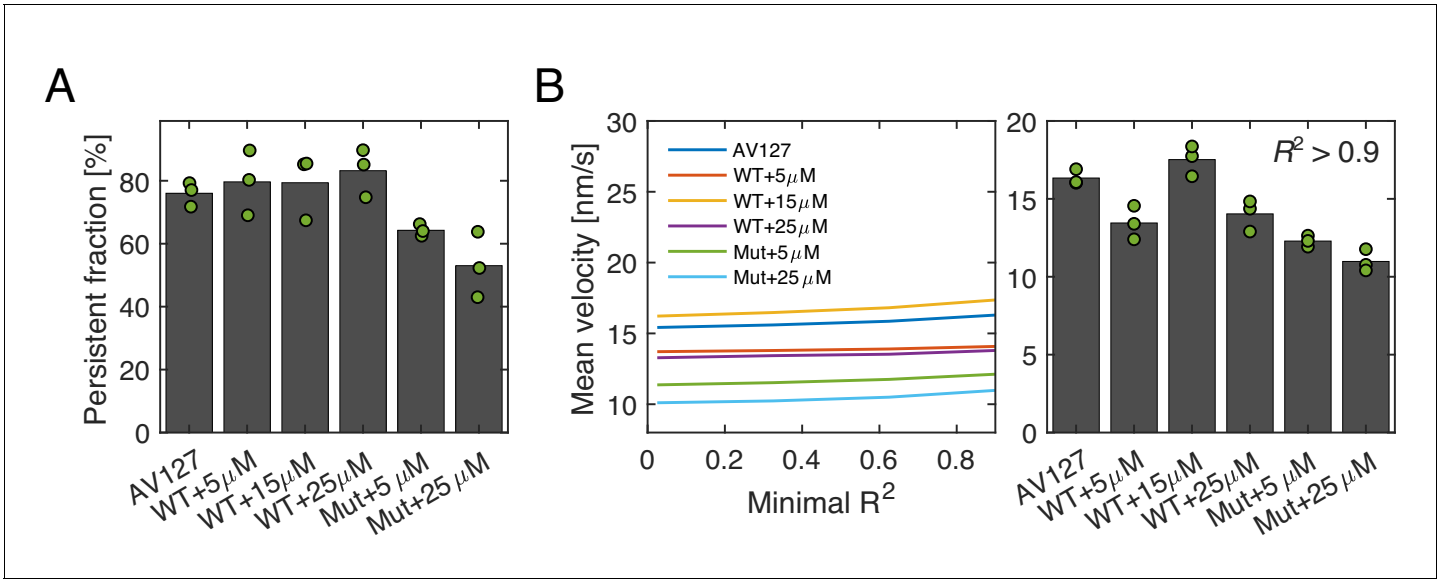

Figure 1—figure supplement 10. Low-frequency tracking of msfGFP-PBP2 and msfGFP-PBP2(L61R) cells under different induction levels. (**A**) Persistent fractions for different expression levels of msfGFP-PBP2 and msfGFP-PBP2(L61R). (**B**) Left. Mean velocity as a function of minimal R^2, which are obtained from a quadratic fit to single-track MSD's of the form $y = a + bx^2$. Right. Mean velocity of tracks, which satisfy $R^2 > 0.9$. Dots represent biological replicates.

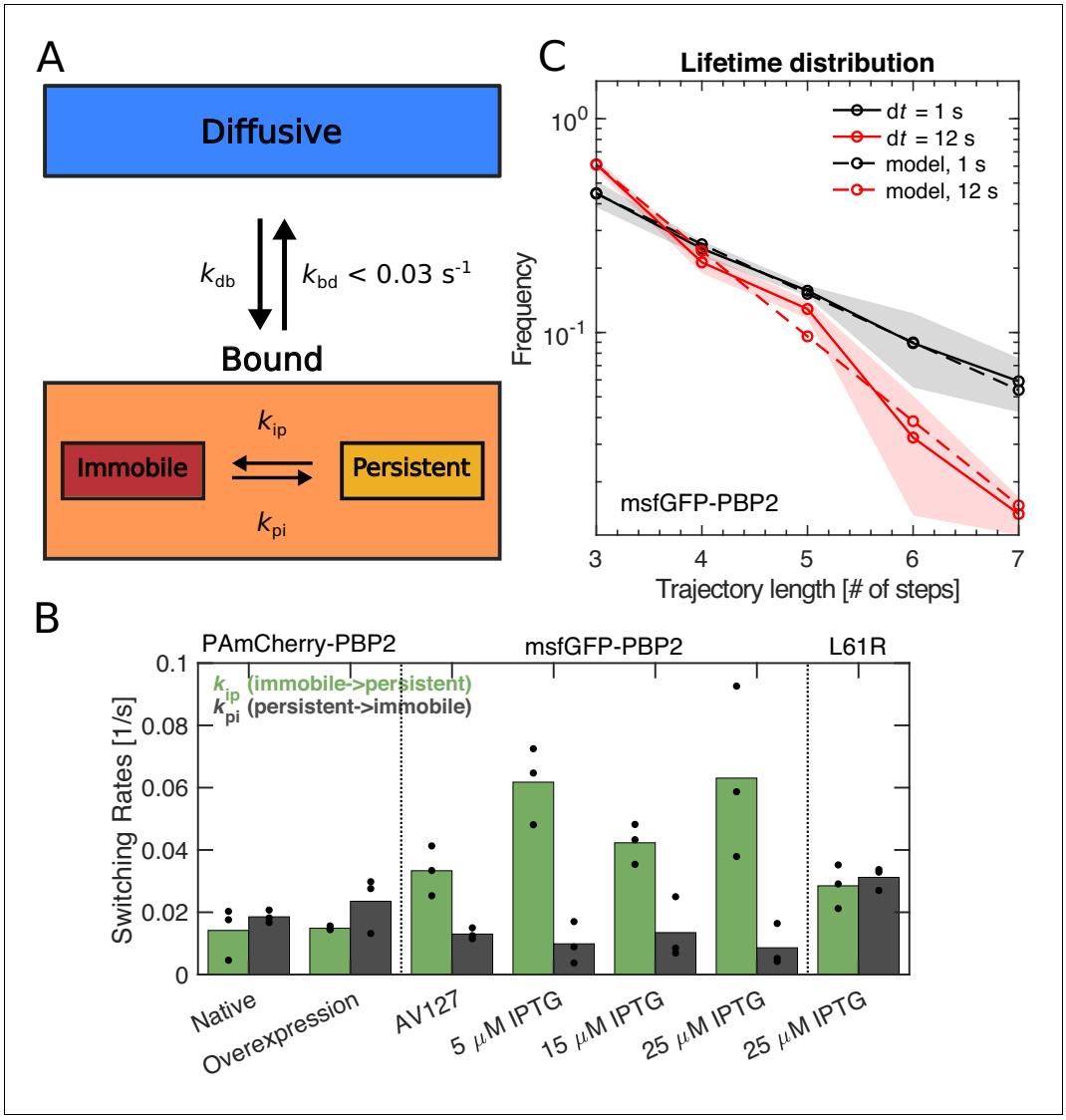

Figure 2. PBP2 molecules transition between different dynamic states. (**A**) Diagram illustrating transition rates measured between different motion states. (**B**) Transition rates between immobile and persistently moving states for different protein fusions and expression levels. Circles: biological replicates. (**C**) Fluorescence-lifetime distributions of msfGFP-PBP2 trajectories with imaging intervals of 1 s (black solid line) and 12 s (red solid line). Dashed lines represent a joint fit of the two curves to a model of photobleaching and bleaching-independent track termination, the latter comprising unbinding and persistently molecules leaving the TIR field of view (bleaching probability per frame p_b = 0.39 ± 0.08, apparent track termination rate k_a = 0.035 ± 0.007 s^{-1}). Based on a model for persistent motion, we obtained an upper limit of the unbinding rate of k_{bd} <0.03/s (***Figure 2—figure supplement 1***). Shaded region: Standard deviation between at least three technical replicates.

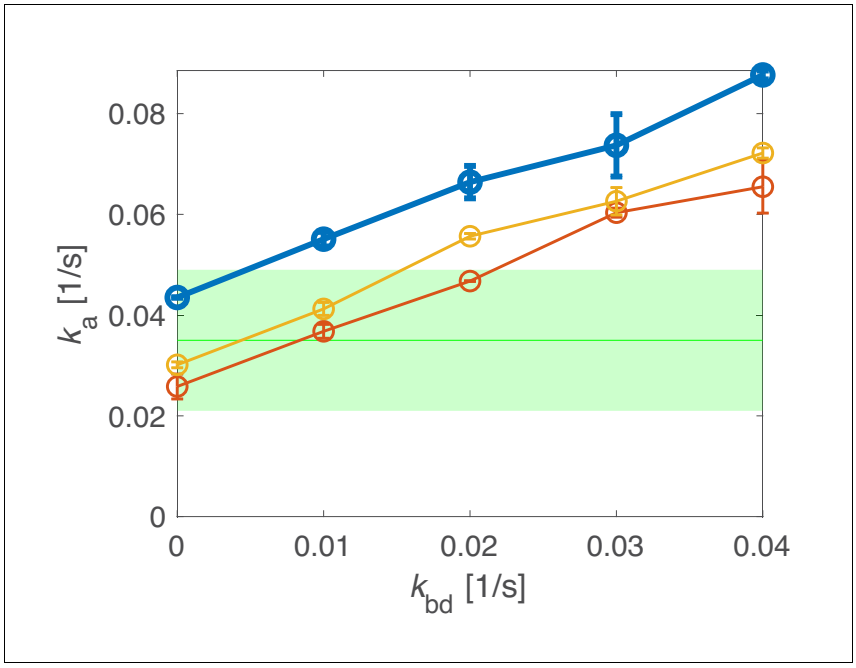

Figure 2—figure supplement 1. Determination of an upper limit of the unbinding rate k_{bd} through simulations. Simulations of track-length distributions reveal the apparent track termination rate k_a as a function of the unbinding rate k_{bd} for different transition simulated rates k_{ip}, k_{pi}. Top: k_{ip} = 0.063/s, k_{pi} = 0.0086/s (experimentally measured rates, leading to a bound fraction of 88%); middle and bottom (thin solid lines): k_{ip} = 0.063/s, k_{pi} = 0.0158/s; k_{ip} = 0.033/s, k_{pi} = 0.0086/s. For the thin solid lines, we adjusted either of the two rates to yield the experimentally measured bound fraction of 80%. Comparison with the experimentally measured apparent unbinding rate (green) allows us to infer an upper bound for the unbinding rate k_{bd} < 0.03/s. Shaded area: 95% confidence interval.

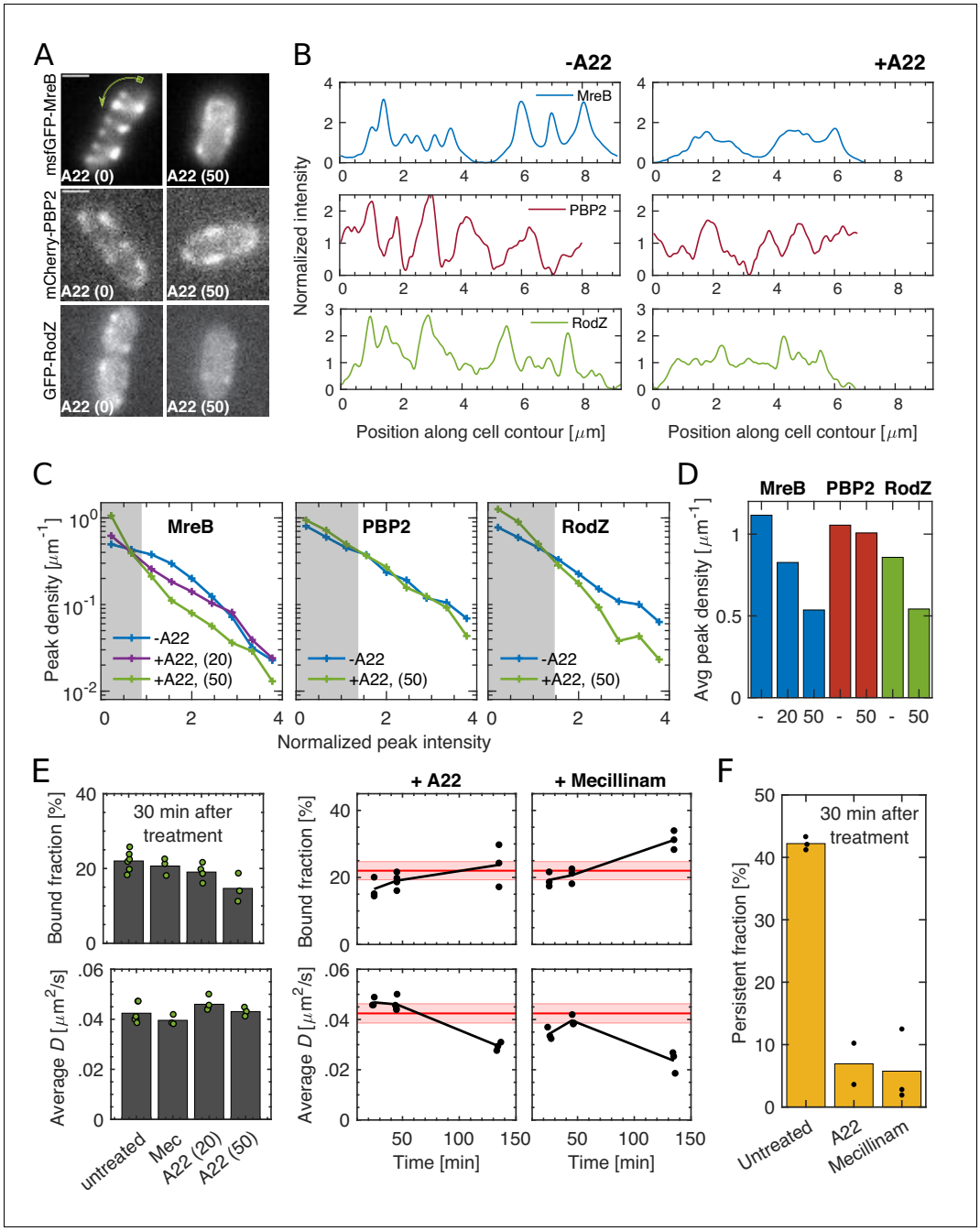

Figure 3. Spatial distribution and magnitude of PBP2 bound fraction are independent of MreB cytoskeleton. (**A–B**) 30 min A22 treatment (50 μg/ml) visibly reduces peak number and intensity of MreB-msfGFP and GFP-RodZ but not of mCherry-PBP2 on cell boundaries, as seen in epi-fluorescence images (**A**) and in line profiles measured along the cell contour (**B**), starting from one cell pole at x = 0 as indicated by the green arrow in (**A**). Image exposure time 1 s. Scale bar 1 μm. (**C**) Peak density on the cell boundary [1/μm] as function of peak intensity for two A22 concentrations (20, 50 μg/ml). Intensities are normalized by median peak intensity in untreated cells. Gray regions: peaks within noise floor. (**D**) Density of all peaks above noise floor in (**A**) for untreated and A22-treated conditions. (**E**) Left. Bound fraction and diffusion constant of PAmCherry-PBP2 30 min after drug treatment with mecillinam (labeled 'Mec', 100 μg/ml) or A22 (20 or 50 μg/ml). Right. Bound fraction and diffusion constant over time after treatment with A22 (20 μg/ml) or mecillinam (100 μg/ml). Dots indicate technical replicates. Red lines and shaded areas: Average values and standard deviations between biological replicates from untreated cells. (**F**) Persistent fractions corresponding to the 30 min time point in (**E**).

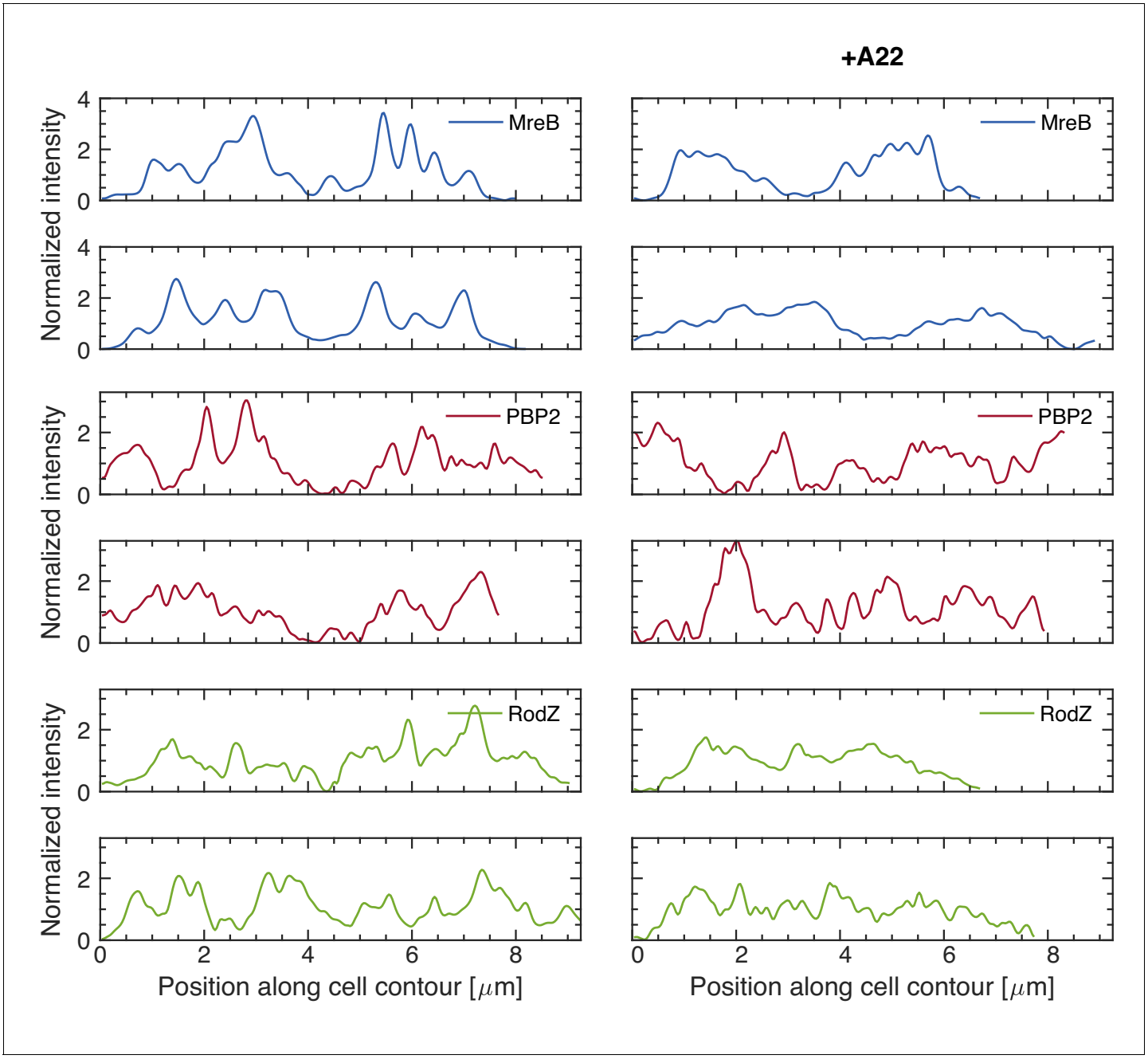

Figure 3—figure supplement 1. Sample fluorescence profiles on cell boundaries as in ***Figure 3B***. Fluorescence profiles along contours of different cells carrying mCherry-PBP2, MreB-msfGFP, or GFP-RodZ fusions for untreated (left) or A22 treated cells (50 µg/ml) (right), obtained in the same way as in ***Figure 3A,B***. Intensities are normalized by the median value and smoothened with a Gauss filter with standard deviation of 33 nm (0.5 pixel).

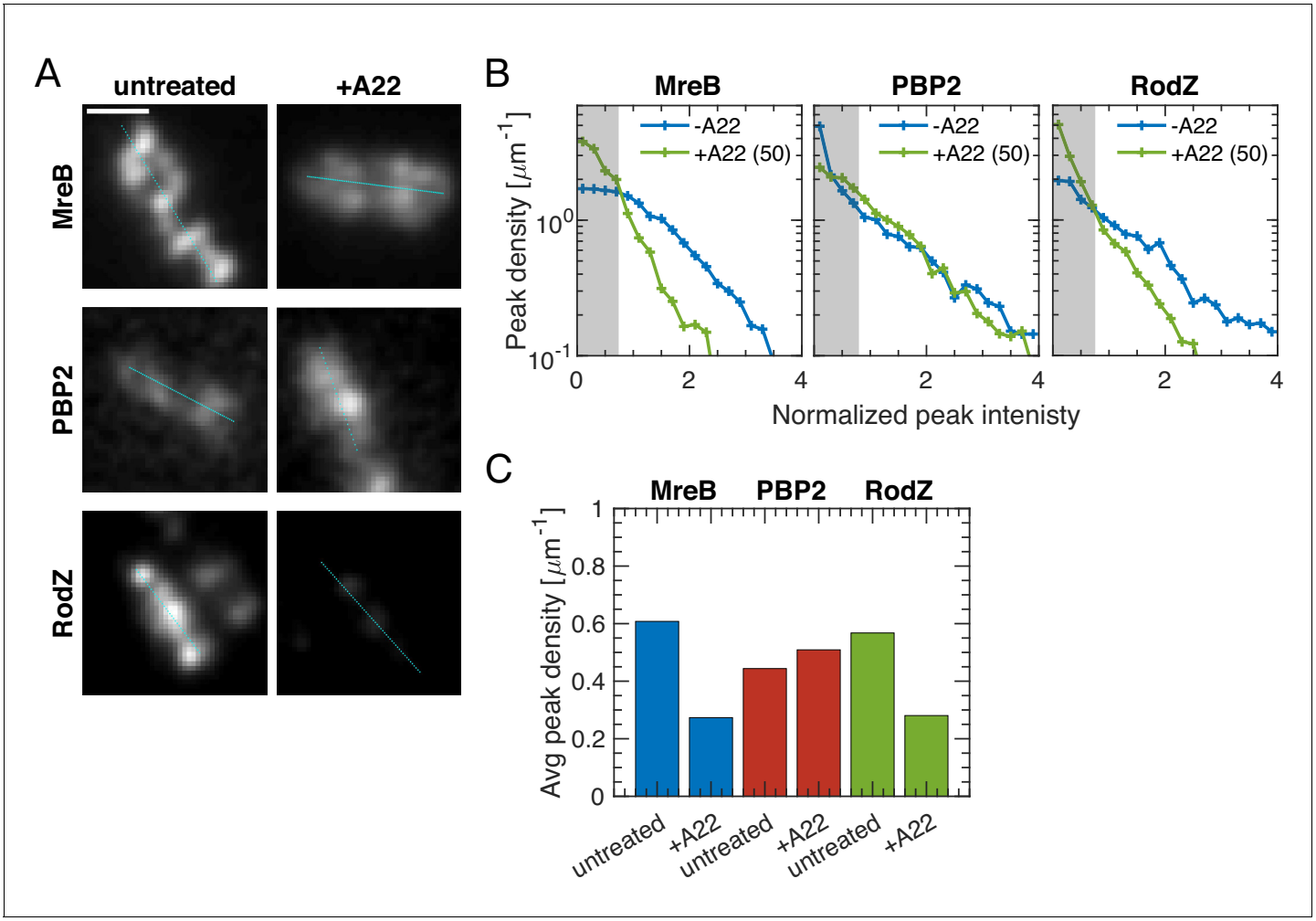

Figure 3—figure supplement 2. Spotty patterns of MreB, RodZ and PBP2 in TIRF microscopy. (**A**) Sample TIRF images with cell centerline plotted in cyan. Scale bar 1 um. (**B–C**). In analogy to ***Figure 3C–D***, TIRF microscopy shows that A22 (30 min; 50 µg/ml) visibly reduces peak number and intensity of MreB-msfGFP and GFP-RodZ but not of mCherry-PBP2.

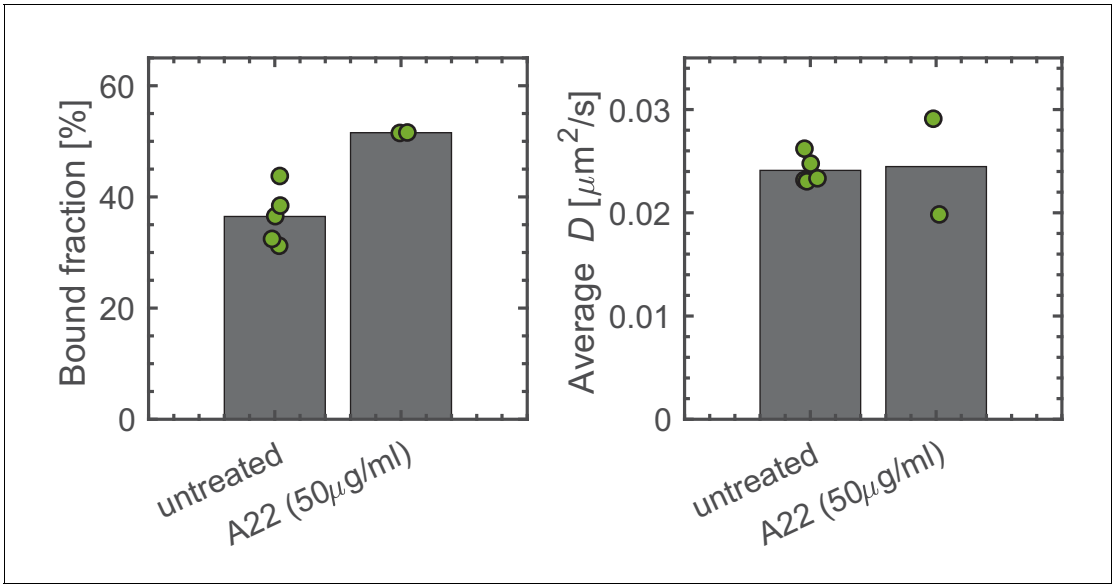

Figure 3—figure supplement 3. Verification of bound fraction measurements with A22 treated cells carrying the msfGFP-PBP2 fusion. Bound fractions and average diffusion constants for untreated and A22-treated (for 30 min) cells carrying the msfGFP-PBP2 fusion (AV127). Dots represent biological replicates.

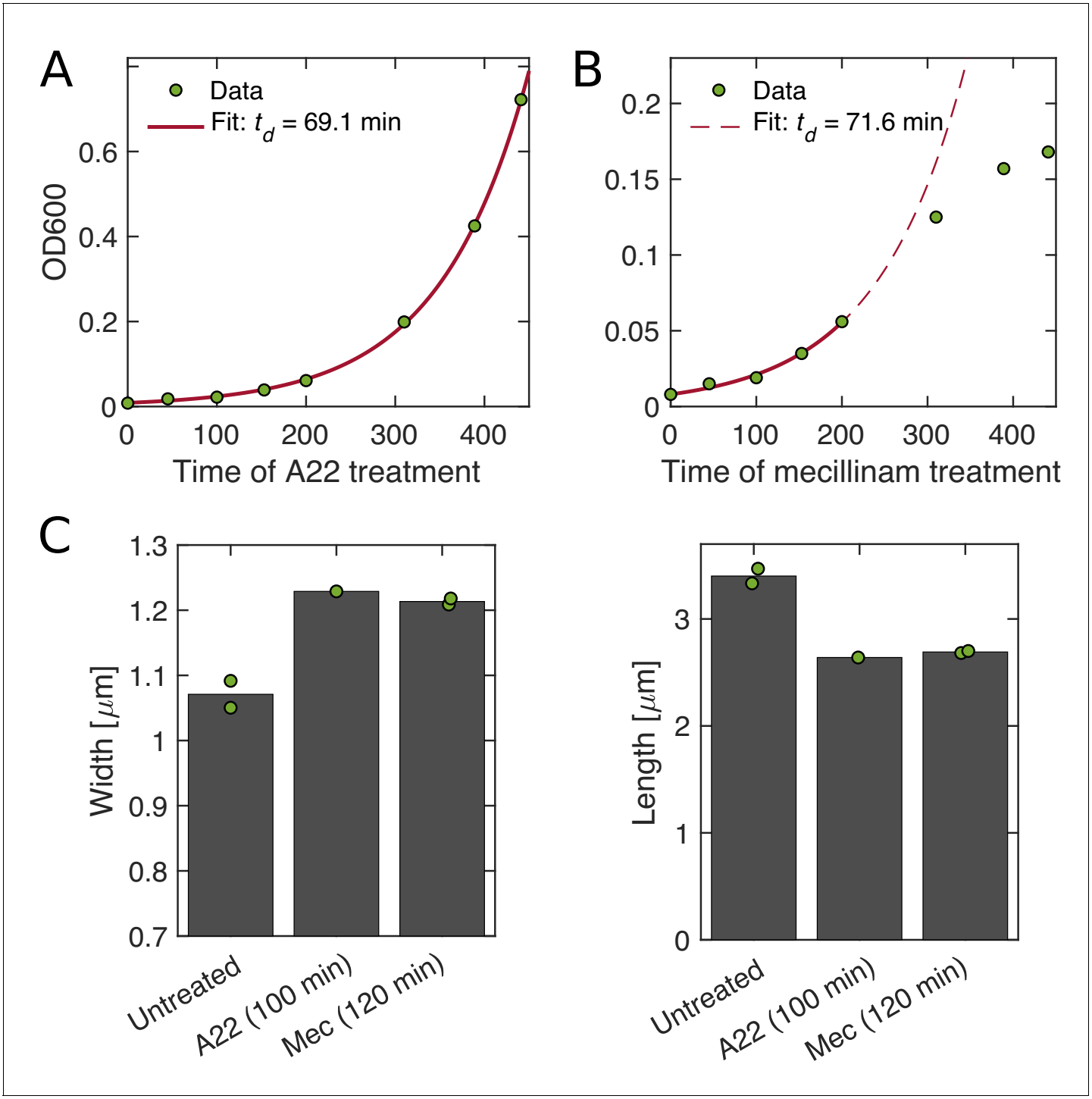

Figure 3—figure supplement 4. Growth and shape of A22- and mecillinam-treated cells. (**A–B**) A22-treated cells grow unperturbed for six generations (**A**), while cells treated with mecillinam show a reduced growth rates after around three generations (**B**). (**C**) Cell shape of cells treated with A22 (**A**) and mecillinam (**B**). In both cases, cells become wider and shorter. Dots represent technical replicates.

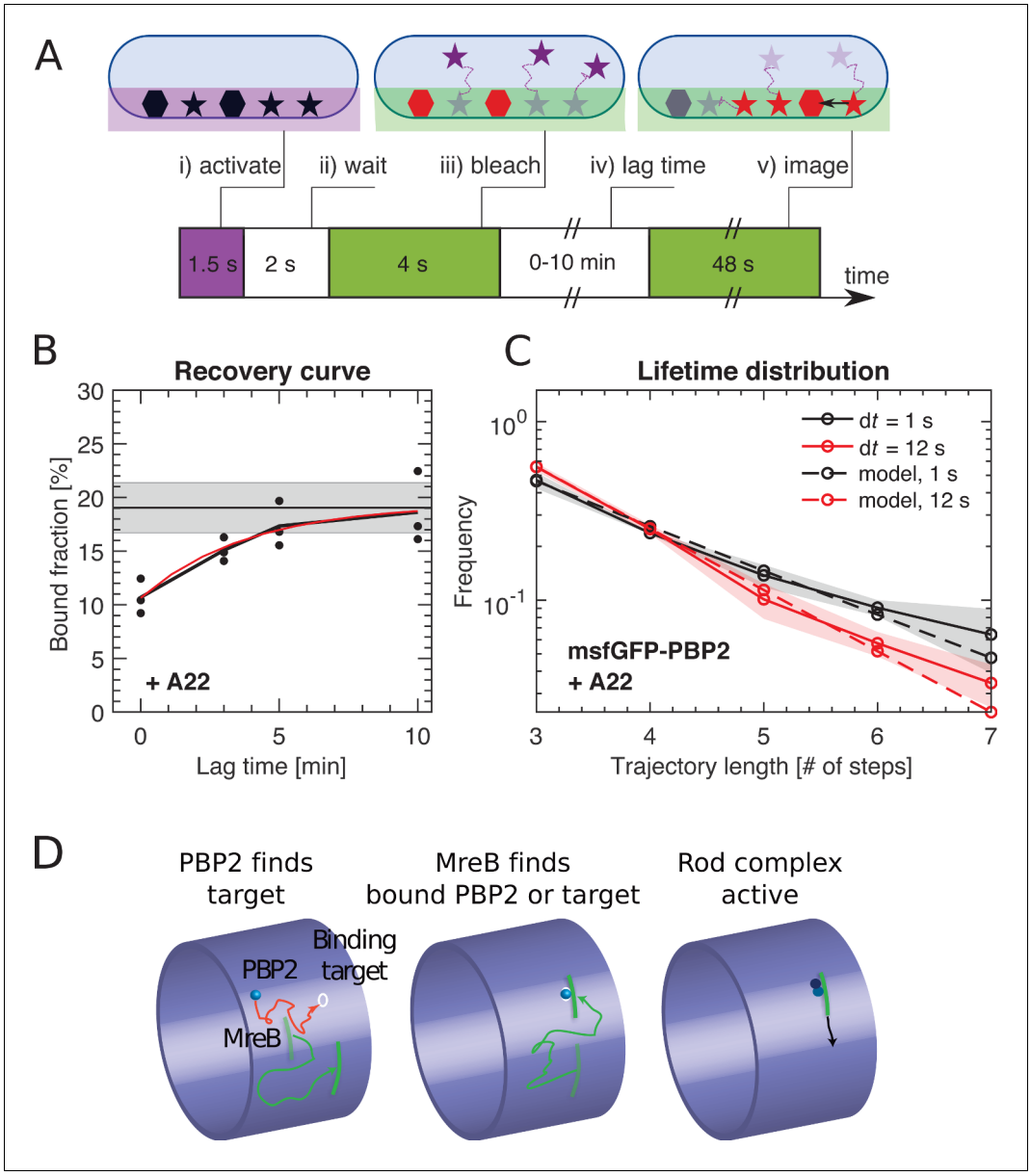

Figure 4. PBP2 slowly transitions between diffusive and bound states. (**A**) Bound-Molecule-FRAP reveals rate of PAmCherry-PBP2 binding k_{db}: (i) Diffusive (stars) and bound (hexagons) molecules are activated at bottom of cell through TIR illumination. (ii) Most activated diffusive molecules (purple) leave the field of view. (iii) Remaining molecules are bleached (red). (iv) Activated diffusive molecules partially return into the field of view, where they can bind (black arrow). (v) Measurement of bound fraction. (**B**) Bound fraction of PAmCherry-PBP2 in A22-treated (20 µg/ml) cells according to (**A**) at different lag times. Black horizontal line and shaded area: bound fraction without bleaching and standard deviation from technical replicates. An exponential fit in the form $b(t) = a_1 - a_2 \exp[-k_{db}\, t]$ (red line) yields binding rate $k_{db} = (4.3 \pm 2)*10^{-3}\ s^{-1}$. Dots represent technical replicates. Shaded area shows standard deviation between six biological replicates. (**C**) Fluorescence-lifetime distributions of msfGFP-PBP2 tracks in A22-treated cells with imaging intervals of 1 s (black solid line) and 12 s (red solid line) yields unbinding rate $k_{bd} = 0.02 \pm 0.01\ s^{-1}$. Shaded area shows standard deviation between at least three technical replicates. (**D**) Cartoon of suggested Rod-complex initiation: PBP2 (blue) binds to a target site in the cell envelope (white circle) independently of MreB filaments or PBP2 activity. PBP2 or the target site then recruits an MreB filament through diffusion and capture (green) or through nucleation, and also recruits other rod-complex components (magenta).

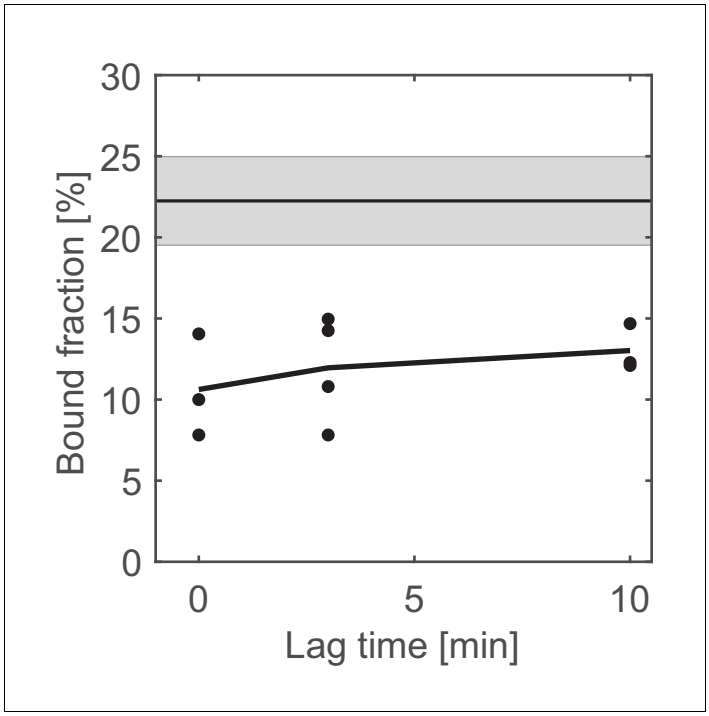

Figure 4—figure supplement 1. Change in the bound fraction after photobleaching of untreated cells. The horizontal line corresponds to the mean bound fractions obtained from unbleached cells (see ***Figure 3***). Error bars and shaded area show standard deviations between at least three technical replicates.

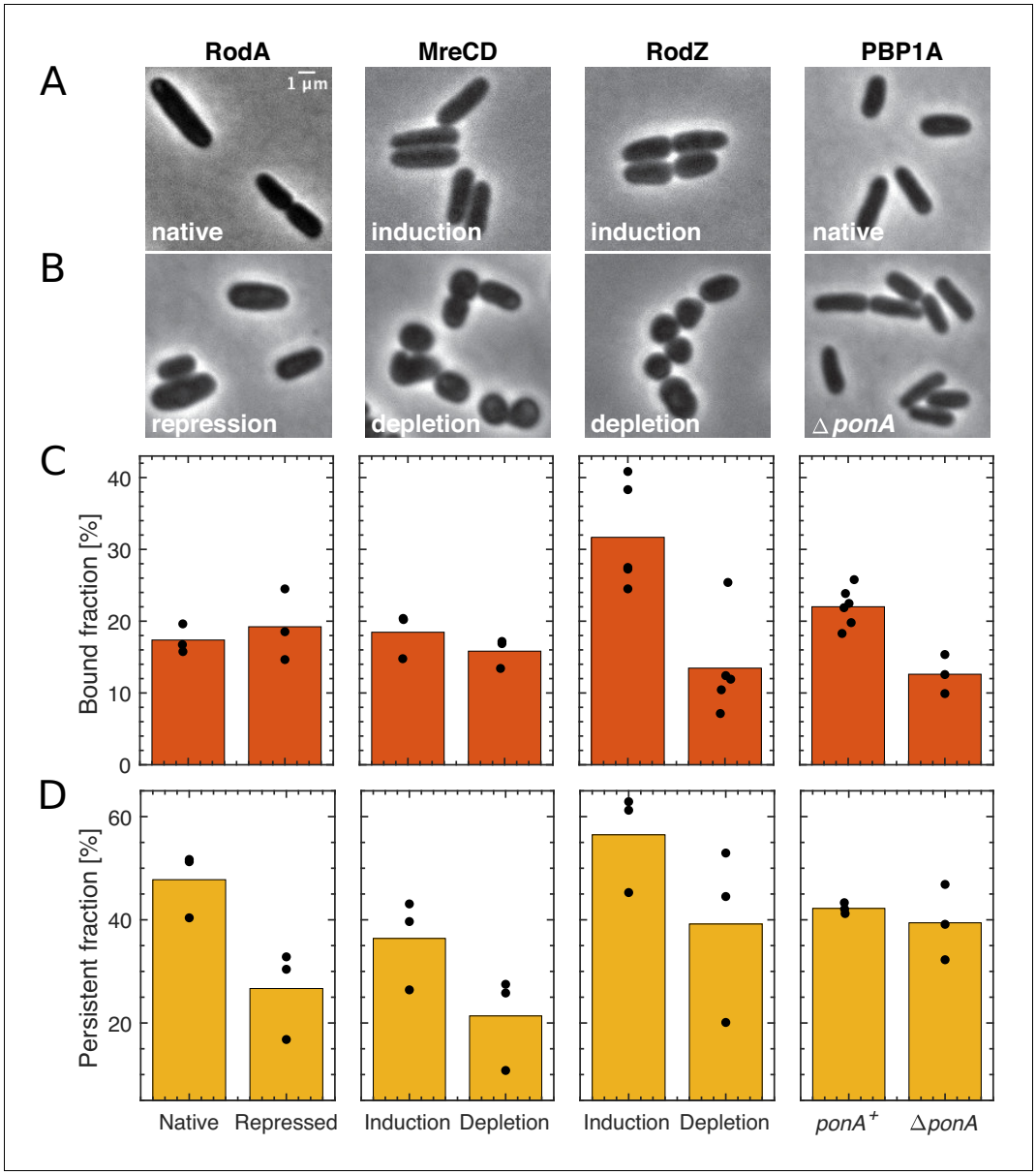

Figure 5. The effect of the depletion of Rod-complex components on PBP2 binding and activity. (**A–B**) Cell shape upon near-native expression (**A**) or long-time depletion (**B**) of RodA, MreCD, RodZ, or PBP1a. RodA was repressed for 9 hr through CRISPRi against *mrdAB* operon (coding for PBP2 and RodA) in AV48/pKC128 [P_{mrdA}::*PAmCherry-PBP2*]. Here, PBP2 was 2–5-fold overexpressed from plasmid pKC128 to avoid PBP2 depletion upon *mrdAB* repression. MreCD was depleted for 6 hr in TKL130 Δ*mreCD*/pFB121 [P_{lac}::*mreCD*]. RodZ was depleted for 6 hr in TKL130 Δ*rodZ*/pFB290 [P_{lac}::*rodZ*]. PBP1a is not essential and was deleted. In all cases except for PBP1A, cells loose rod-like cell shape. (**C–D**) Bound fractions (**C**) and persistent fractions (**D**) of PAmCherry-PBP2 upon expression or depletion of proteins indicated above (**A**). Dots represent biological replicates.

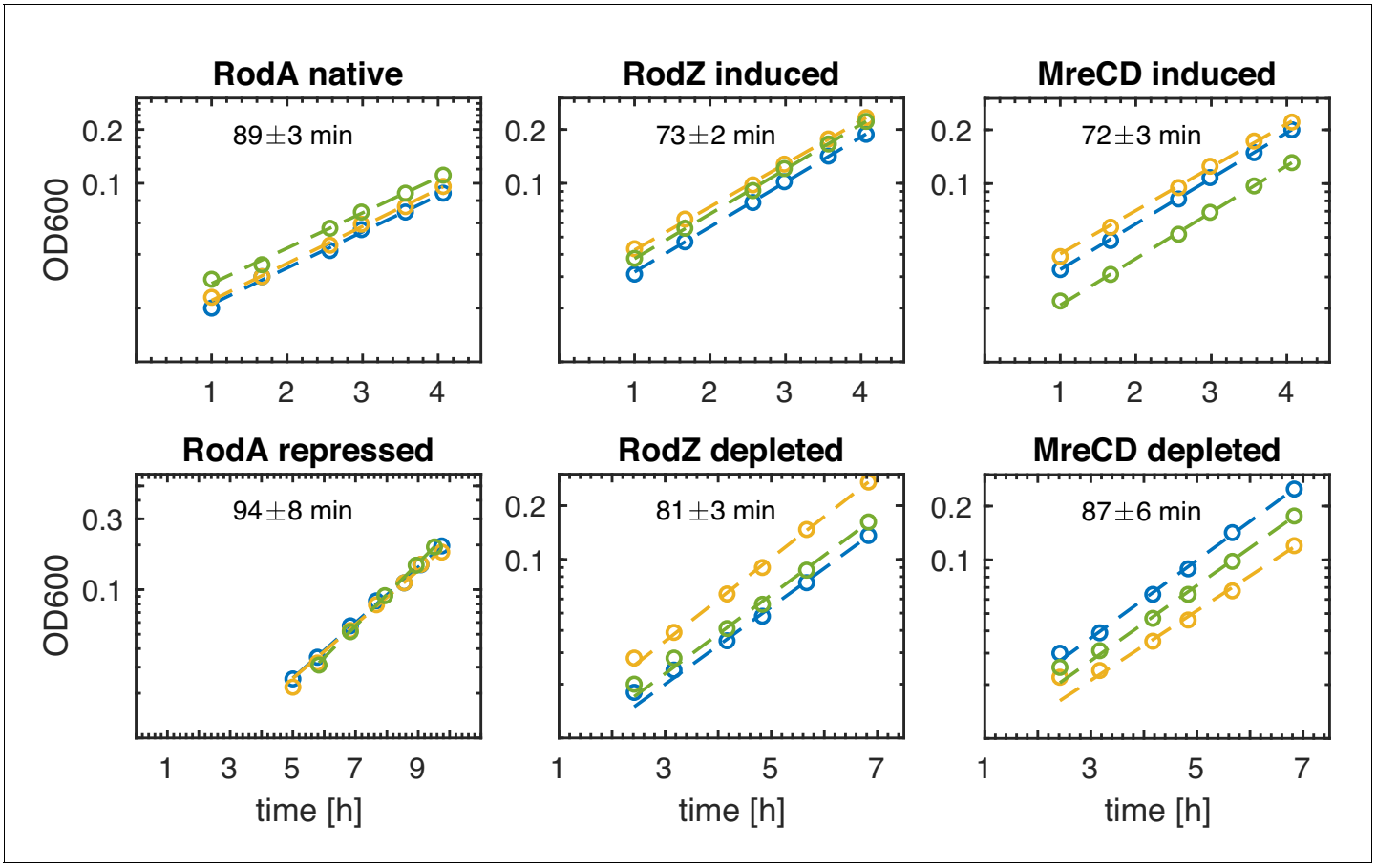

Figure 5—figure supplement 1. Depletion of Rod-complex components shows no effect on growth. Growth curves for the different depletion strains in induced and depleted conditions as a function of time after initiating protein depletion. The doubling time is obtained from an exponential fit. three biological replicates for each condition. Y-axis is shown in log-scale.

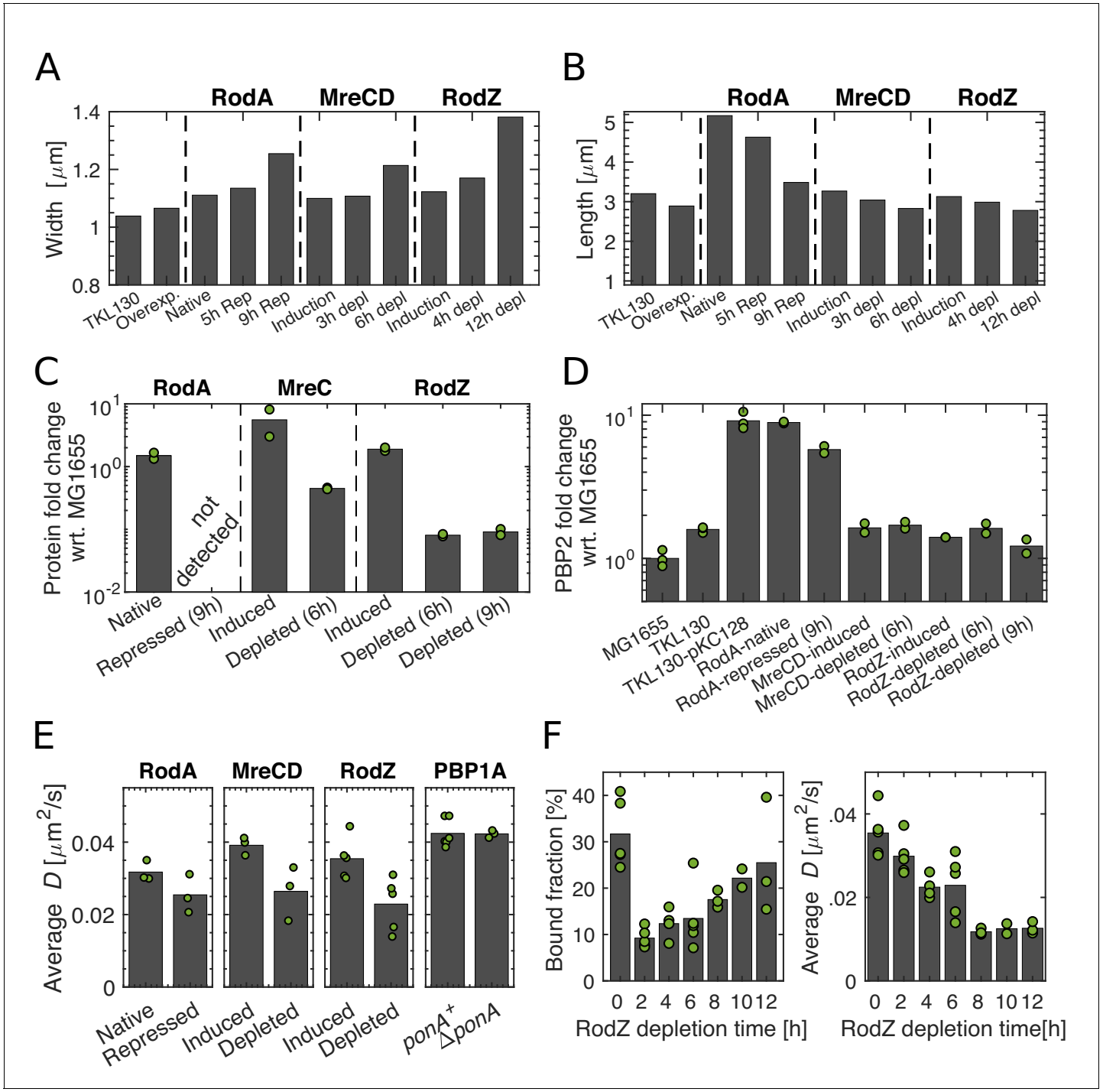

Figure 5—figure supplement 2. Depletion of Rod-complex components. (**A–B**) Cell length and width upon repression of RodA, and depletion of MreCD or RodZ at different time points after initiating protein depletion. (**C–D**) Levels of RodA, MreC, and RodZ (**C**) and levels of PBP2 (**D**) acquired by mass spectrometry (DIA). Protein levels are normalized by the mean of the corresponding protein level in MG1655. Dots represent two biological replicates for each condition. (**E**) Average diffusion constants drop upon repression of potential members of the Rod complex. Dots represent biological replicates. (**F**) Bound fraction and average diffusion constant of PBP2-PAmCherry at different time points during RodZ depletion. Dots represent biological replicates.

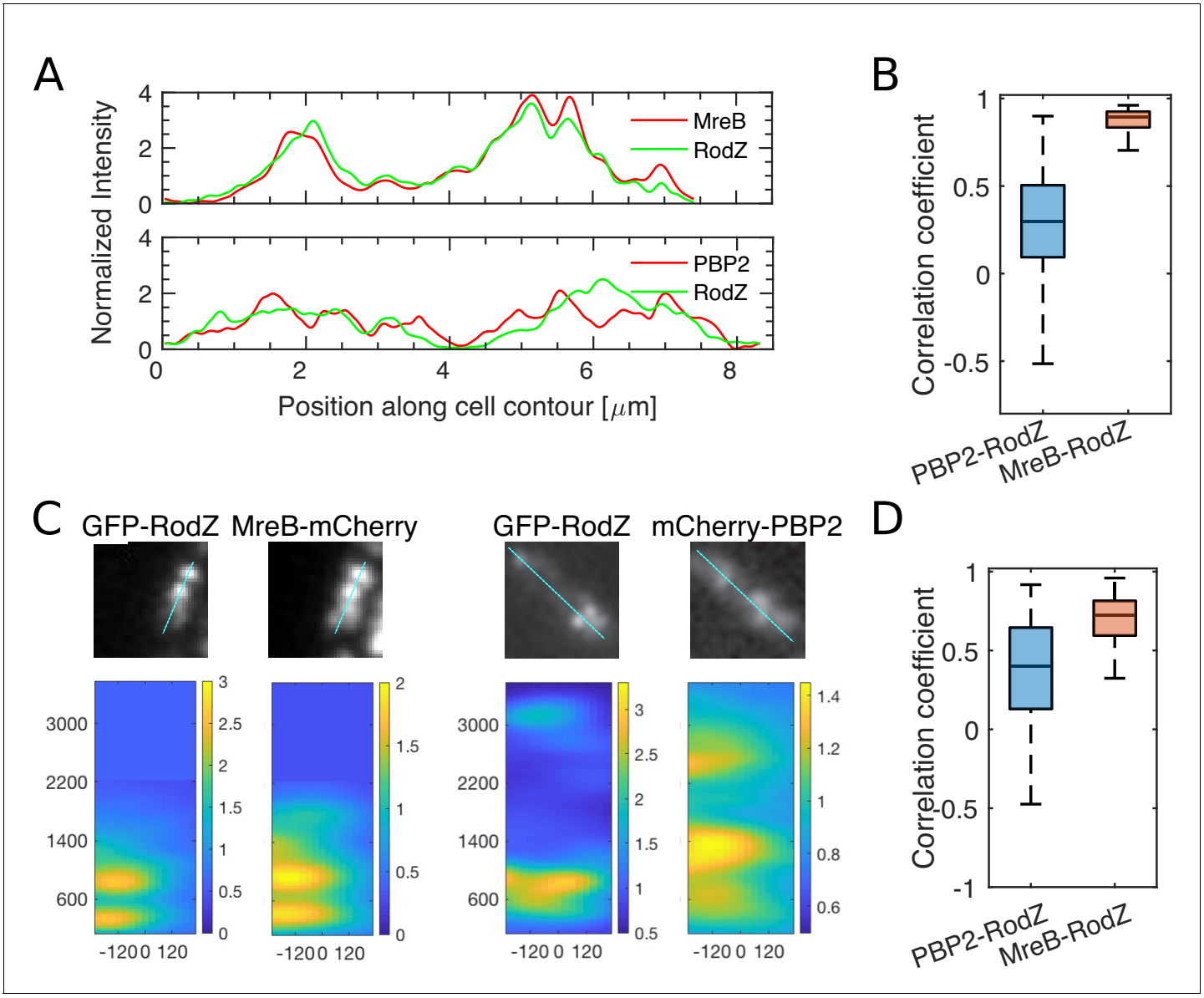

Figure 5—figure supplement 3. RodZ and PBP2 do not colocalize, while RodZ and MreB do. (**A**) Sample profiles along the cell centerline of different cells carrying MreB-mCherry and GFP-RodZ fusions (Δ*rodZ mreB* <> *mreB* mCherry (P_{lac}::*gfp-rodZ*)) (top) or mCherry-PBP2 and GFP-RodZ fusions (Δ*rodZ mrdA* <> *mCherry* mrdA (P_{lac}::*gfp-rodZ*)) (bottom) acquired by epi-fluorescence microscopy. Intensities are normalized by the median value and then smoothened with a Gauss filter with standard deviation of 33 nm (0.5 pixel). (**B**) Boxplots of Pearson correlation coefficients between PBP2- and RodZ signals (left) and between MreB-and RodZ signals (right) acquired by epi-fluorescence microscopy. (**C**) Sample snapshots and corresponding intensity maps of cells carrying mCherry-PBP2 and GFP-RodZ fusions (Δ*rodZ mrdA* <> *mCherry* mrdA (P_{lac}::*gfp-rodZ*)) (left) or MreB-mCherry and GFP-RodZ fusions (Δ*rodZ mreB* <> *mreB* mCherry (P_{lac}::*gfp-rodZ*)) (right) acquired by TIRF microscopy. Intensities are normalized by the median value. x-axis show position along the short axis of the cell where zero corresponds to the centerline (mid-cell). y-axis is then the position along the cell's long axis. Distances are given in nm. Scale bar shows 1 um. Intensity maps are stretched in x-direction for better visibility. (**D**) Boxplots of Pearson correlation coefficients between PBP2- and RodZ signals (left) and between MreB-and RodZ signals (right) acquired by TIRF microscopy.

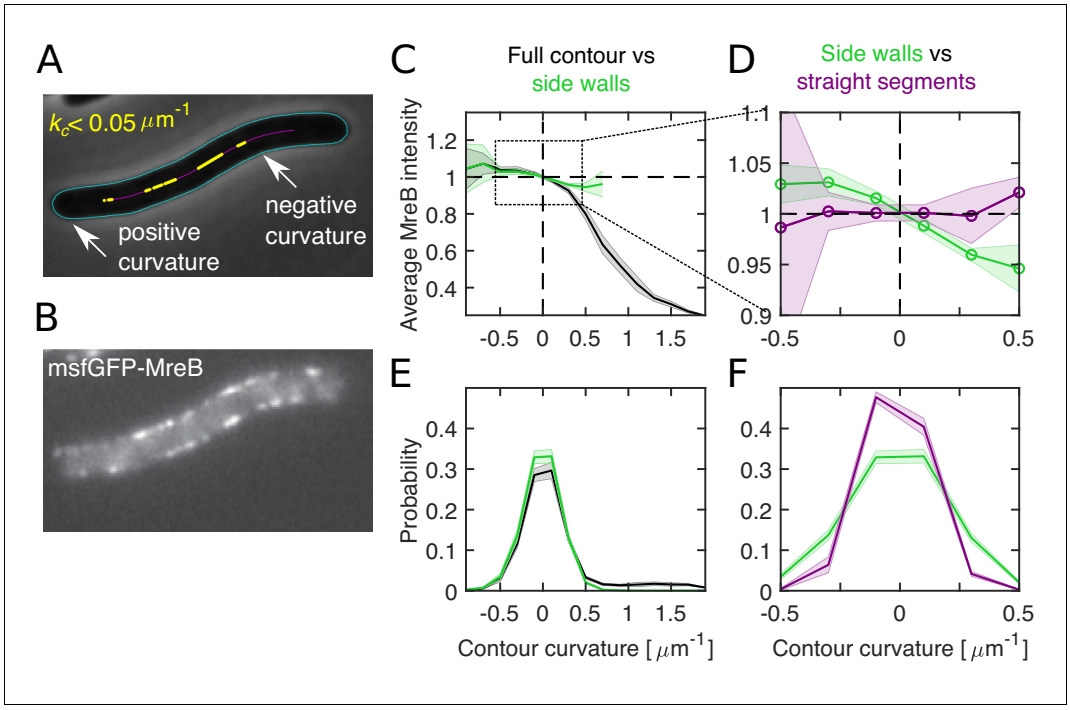

Figure 6. Differential MreB-curvature correlations in filamentous cells are due to cell poles and cell bending. (**A–B**) Phase-contrast image (**A**) and fluorescence intensity (**B**) of a representative filamentous *E. coli* expressing MreB-msfGFP and SulA (NO53/pDB192). Contours (cyan) are obtained by computational cell segmentation. Positive contour curvature is found at cell poles, bulges, and outer parts of spontaneously bent regions, while negative curvature is found at indentations and inner parts of bent regions. Straight cell segments (yellow) are defined as regions where the curvature of the spatially averaged centerline (magenta) is smaller than 0.05 μm^{-1}. (**C–D**) Normalized average MreB intensity as a function of local contour curvature. Comparison between correlations obtained from full contours (black) and side walls (green) (**C**) and from side walls (green) and straight cell segments (magenta) (**D**). (**E–F**) Distributions of contour-curvature values corresponding to correlation plots in (**C–D**). Shaded region: Standard deviation between three biological replicates.

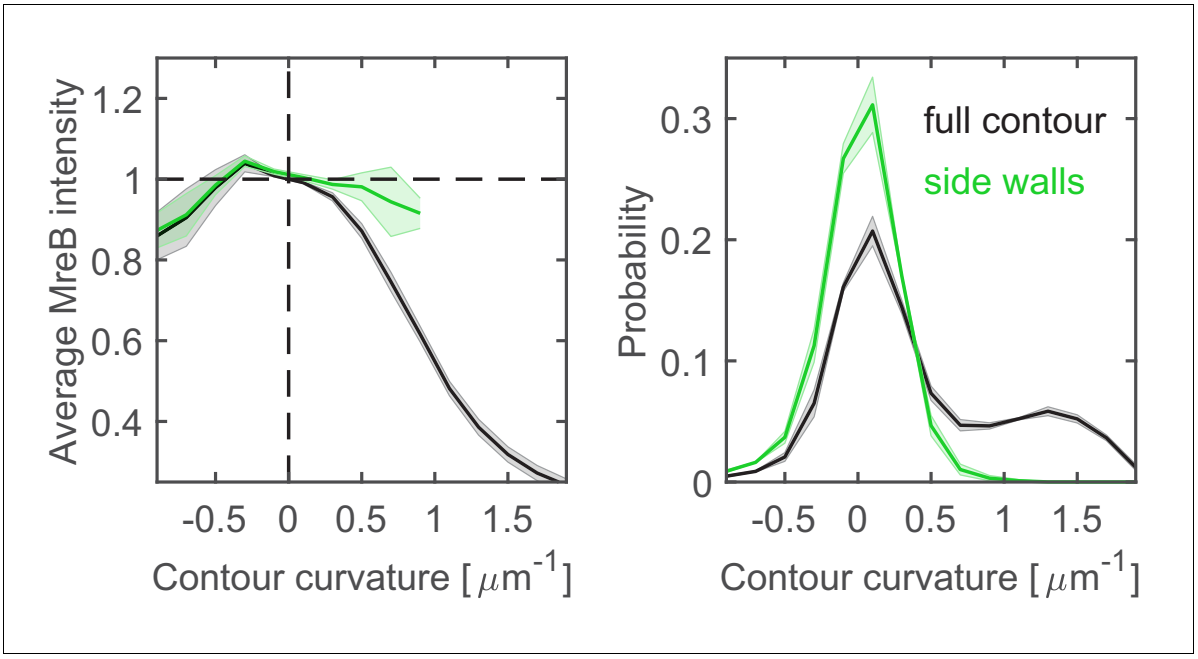

Figure 6—figure supplement 1. Correlations between MreB and contour curvature in WT cells. Left. Normalized average MreB intensity as a function of local contour curvature in strain NO53 (*mreB* <> *mreB* msfGFP). Comparison between correlations obtained from full contours (black) and side walls (green). Right. Distributions of contour-curvature values corresponding to correlation plots on the left. Shaded areas show standard deviation between three biological replicates.

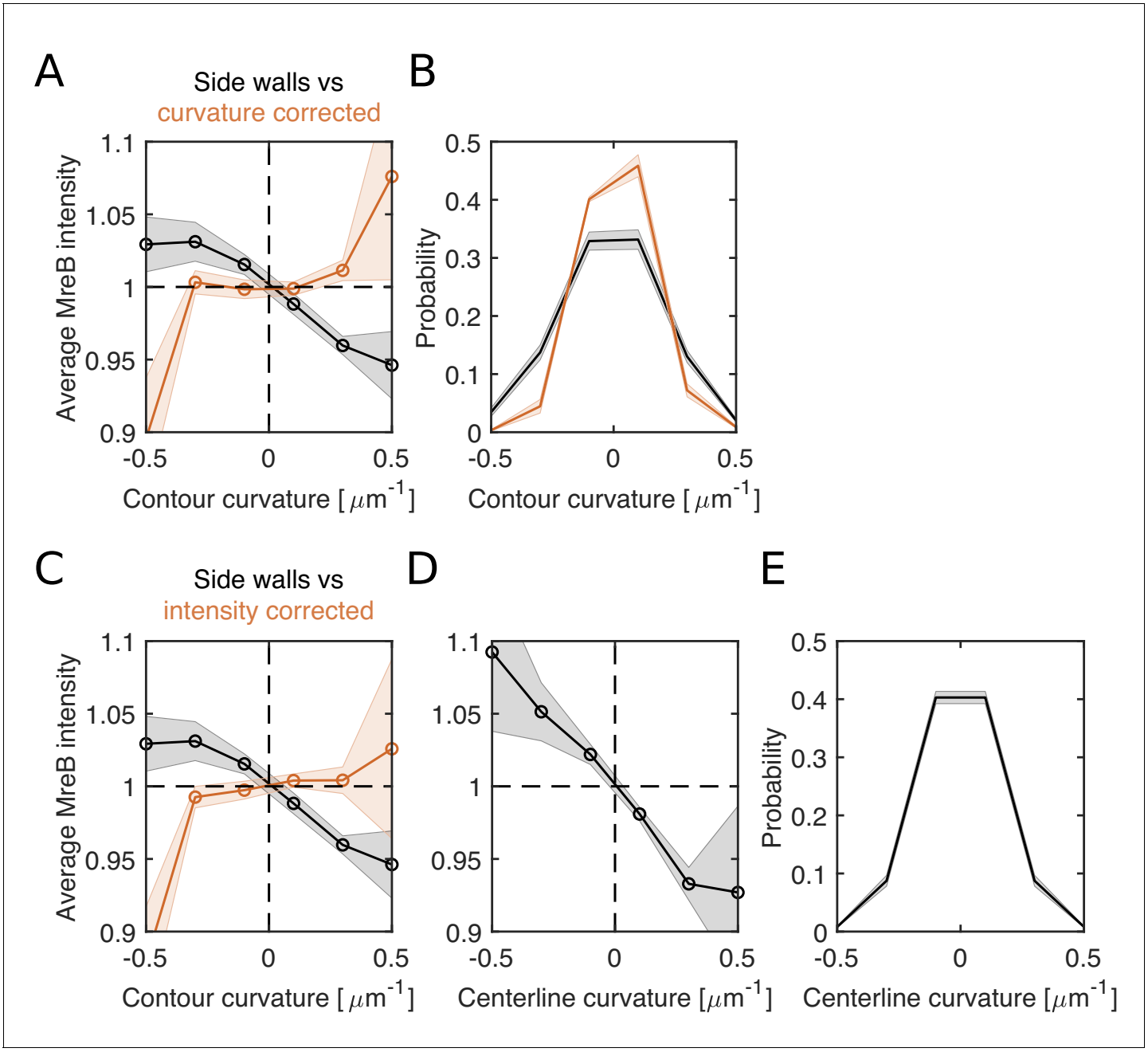

Figure 6—figure supplement 2. Loss of correlations between MreB and contour curvature after renormalizing either curvature or intensity for cell bending in filamentous cells. (**A–B**) Curvature correction. (**A**) Average MreB intensity as a function of contour curvature (black) and bending-corrected contour curvature (orange) in NO53/pDB192 (P_{lac}::*sulA*). (**B**) Distributions of contour curvature (black) and corrected contour curvature (orange). Curvature correction leads to a narrower distribution while ~ 80% of local curvature values keep their original sign of curvature. (**C–E**) Intensity correction. (**C**) Average MreB intensity as a function of bending-corrected MreB-intensity (orange). Intensity is corrected for observed correlations between MreB intensity and centerline curvature in (**D**) (Materials and methods). (**D**) Average MreB intensity as a function of smoothened centerline curvature (using a Gauss filter of σ = 80 nm). (**E**) Centerline-curvature distribution. Shaded areas show standard deviation between three biological replicates.

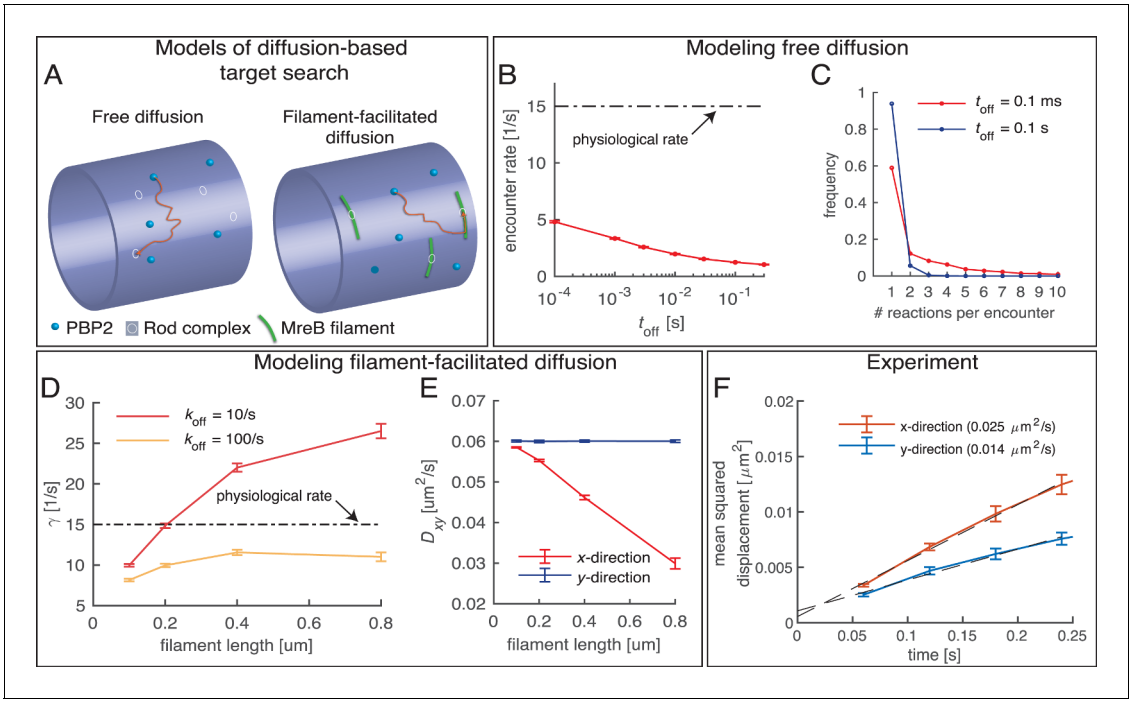

Figure 7. Testing a possible role of diffusive PBP2 for cross-linking. (**A**) Cartoon of PBP2 finding the target site of a 'rod complex' through free diffusion (left) or filament-facilitated diffusion (right). (**B**) The average encounter rate between any of 100 freely diffusing PBP2 molecules and a given rod-complex site as a function of the unknown latency time t_{off} (the duration for which a single PBP2 enzyme is inactive after a cross-linking reaction) (red) in comparison to the physiological cross-linking rate (dashed-dotted line) (**C**) Distribution of the number of successive cross-linking reactions conducted by the same PBP2 molecule at the same rod-complex site for two different latency times. (**D–E**) Facilitated diffusion along circumferentially oriented filaments centered at every rod-complex site increases the encounter rate (**D**) and renders diffusion asymmetric (**E**). (**F**) Diffusion of PAmCherry-PBP2 along the long axis of the cell (x-direction) is faster than around the circumference (y-direction), suggesting that PBP2 does not undergo facilitated diffusion along circumferentially oriented filaments. Reduced diffusion around the circumference is possibly caused by out-of-plane motion.